

Spring 5-10-2019

Global Performance Testing, Simulation, and Optimization of a 6-MW Annular Floating Offshore Wind Turbine Hull

Hannah L. Allen

University of Maine, hannah.louise.allen@maine.edu

Follow this and additional works at: <https://digitalcommons.library.umaine.edu/etd>

Part of the [Ocean Engineering Commons](#)

Recommended Citation

Allen, Hannah L., "Global Performance Testing, Simulation, and Optimization of a 6-MW Annular Floating Offshore Wind Turbine Hull" (2019). *Electronic Theses and Dissertations*. 2959.
<https://digitalcommons.library.umaine.edu/etd/2959>

This Open-Access Thesis is brought to you for free and open access by DigitalCommons@UMaine. It has been accepted for inclusion in Electronic Theses and Dissertations by an authorized administrator of DigitalCommons@UMaine. For more information, please contact um.library.technical.services@maine.edu.

**GLOBAL PERFORMANCE TESTING, SIMULATION, AND OPTIMIZATION
OF A 6-MW ANNULAR FLOATING OFFSHORE WIND TURBINE HULL**

By

Hannah Allen

B.S. University of New Haven, 2015

A THESIS

Submitted in Partial Fulfillment of the

Requirements for the Degree of

Master of Science

(in Mechanical Engineering)

May 2019

Advisory Committee:

Andrew J. Goupee, Assistant Professor of Mechanical Engineering, Co-Advisor

Habib J. Dagher, Director of the Advanced Structures and Composites Center,
Bath Iron Works Professor, Co-Advisor

Anthony M. Viselli, Research Assistant Professor and Manager of Offshore
Testing and Design, Advanced Structures and Composites Center

Masoud Rais-Rohani, Chair & Richard C. Hill Professor of Mechanical
Engineering

© 2019 Hannah L. Allen

All Rights Reserved

**GLOBAL PERFORMANCE TESTING, SIMULATION, AND OPTIMIZATION
OF A 6-MW ANNULAR FLOATING OFFSHORE WIND TURBINE HULL**

By Hannah Allen

Thesis Co-Advisors: Dr. Andrew J. Goupee & Dr. Habib J. Dagher

An Abstract of the Thesis Presented
in Partial Fulfillment of the Requirements for the
Degree of Master of Science
(in Mechanical Engineering)
May 2019

Floating offshore wind turbine (FOWT) hull technologies are evolving rapidly with many technically viable designs. However, a commercially dominant architecture has yet to emerge. This thesis presents a methodology for evaluation of the hydrodynamic performance of an annular FOWT hull. This hull shows significant promise from a manufacturing and installation standpoint, but limited performance data exists. This thesis will provide ample documentation on scale model testing of an annular FOWT hull as well as the corresponding numerical validation approach and opportunities for design improvement.

The first portion of this work involves testing a 1/100th-scale model in the Harold Alfond Wind Wave Ocean Engineering Laboratory at the University of Maine's Advanced Structures and Composites Center followed by an investigation of wave-induced motion using ANSYS AQWA, a commercial hydrodynamic software. The experimental and numerical results are compared to determine the ability of ANSYS AQWA to simulate the response of an annular FOWT hull, which here implies that the hull contains a moonpool. The wave-only performance of the annular hull is also

compared to experimental data obtained for other baseline FOWT hulls. In addition to quantifying a baseline hull this thesis will also explore modifications in the annular geometry to further explore the design space in an effort to find a more optimal annular hull configuration for use in FOWT applications.

ACKNOWLEDGEMENTS

I would like to express my sincere gratitude to the generous contributions of the Harold Alfond Foundation which provided the funding for this work. The Foundation's constant support of engineering feats and other areas in Maine does not go unnoticed.

It is difficult to generate a truly complete list of those who have helped me along in this process. Certainly, thanks go out to the offshore team at the University of Maine's Advanced Structures and Composites Center including Chris Allen, Matt Cameron, and Matt Fowler for their support of my model testing efforts as well as helping me navigate the often choppy seas of learning the basics of floating offshore wind. Thank you also to Lindsay Wells and Peter Jalbert for their constant camaraderie and help in model fabrication and other areas. Thanks to the unsung heroes at the Composites Center behind the scenes and out in the lab.

I cannot adequately express my gratitude to my advisor Dr. Andy Goupee for his unwavering support of my learning process as he helped me to fearlessly apply myself to this project without passing on shame for errors made along the way. Thank you to Dr. Habib Dagher and Dr. Anthony Viselli for their continued passion for and support of offshore wind in Maine —both for my own sake and for the sake of Maine's future. I would also like to thank Dr. Masoud Rais-Rohani for believing in me, perhaps more than I have believed in myself at times. Without the dedication of these individuals, this work would most certainly not have been possible.

It is important to me that the support from my family and friends does not go unnoticed. Thanks to the numerous graduate students at the Composites Center among them, in particular, Jacob Ward, William West, Rick Perry, Adam Letourneau, and

Anthony Verzoni. Thank you to my parents Beth and Doug Allen for instilling in me the belief that personal growth is always possible. Thank you to my brother Greg and my sister Meredith for silently challenging me to push myself to keep up with their high standards and determination. Finally, thank you to Kaitlyn Bartlett for her fierce belief that I could make this a reality and for her ability to handle the crazy schedule and other realities that have come with this quest.

TABLE OF CONTENTS

ACKNOWLEDGEMENTS	iii
LIST OF TABLES	ix
LIST OF FIGURES	x
LIST OF NOMENCLATURE	xiii
LIST OF ACRONYMS AND ABBREVIATIONS	xv
CHAPTER 1 INTRODUCTION	1
1.1. Motivation.....	1
1.2. Background	2
1.2.1. Existing and in-the-Works Floating Offshore Wind Turbines	3
1.2.2. Use of Froude Scaling to Derive Equivalent 6-MW Systems	11
1.2.3. Moonpools	15
1.3. Research Contributions.....	18
1.4. Thesis Overview	18
CHAPTER 2 EXPERIMENTAL COMPARISON OF AN ANNULAR FLOATING OFFSHORE WIND TURBINE HULL AGAINST PAST MODEL TEST DATA	20
2.1. Introduction.....	20
2.2. Model Description	21
2.3. Testing Environments	25
2.4. Numerical Modeling	26
2.5. Results.....	29

2.5.1. Position RAO Magnitudes	30
2.5.1.1. Low-Energy Position RAO Magnitudes	30
2.5.1.2. High-Energy Position RAO Magnitudes	33
2.5.2. Nacelle Acceleration RAO Magnitudes.....	37
2.5.2.1. Low-Energy Nacelle Acceleration RAO Magnitudes	37
2.5.2.2. High-Energy Nacelle Acceleration RAO Magnitudes.....	39
2.5.3. Impacts of Heave Plate Addition	41
2.6. Discussion	43
2.6.1. Comparison of Response in Low-Energy and High-Energy Sea States	44
2.6.2. Discrepancy between RAO Magnitudes Derived from Irregular Waves and Regular Waves	45
2.6.3. ANSYS AQWA Modeling Capability.....	45
2.6.4. Performance Comparison for Annular Hull and DeepCwind Platforms	45
2.6.5. Influence of Heave Plates on Performance	46
 CHAPTER 3 COMPARATIVE STUDY OF ANNULAR FOWT HULL GEOMETRIES	 47
3.1. Development of Hull Alternatives	47
3.1.1. Shape Variations	47
3.1.2. Stability Requirements and Standardized Parameters	47
3.2. Shape Comparison Resulting Geometries	49

3.3. ANSYS AQWA Parameters	51
3.3.1. Mesh Sizing	51
3.3.2. Modeling Parameters	52
3.3.3. Assumptions and Simplifications	53
3.4. Results.....	54
3.4.1. Natural Periods.....	54
3.4.2. ANSYS AQWA Added Mass.....	55
3.4.3. ANSYS AQWA Response Amplitude Operators.....	58
3.5. Discussion	61
CHAPTER 4 SIZING OPTIMIZATION OF SQUARE ANNULAR HULL	63
4.1. Introduction.....	63
4.2. Optimization Problem Statement.....	63
4.2.1. Objective Functions	64
4.2.2. Design Variables and Corresponding Bounds	65
4.2.3. Constraints	68
4.3. Use of NSGA-II Optimization Technique	69
4.4. Results.....	72
4.5. Discussion	76
CHAPTER 5 CONCLUSIONS AND FUTURE WORK.....	78
5.1. Conclusions.....	78
5.2. Future Work	79
REFERENCES	81
APPENDIX A: Optimization MATLAB functions	86

APPENDIX B: Optimization Generation 100 Population.....	105
BIOGRAPHY OF THE AUTHOR.....	108

LIST OF TABLES

Table 1.1. Wind turbine scaling guidelines	12
Table 1.2. 6-MW Froude Scaling information.....	12
Table 2.1. Select model specifications.....	23
Table 2.2. Regular wave characteristics	26
Table 2.3. Broadband wave characteristics.....	26
Table 3.1. Shape variation standardized parameters.....	48
Table 3.2. Selected resulting parameters	50
Table 3.3. Shape variation inertias and center of gravity locations	51
Table 3.4. Mesh characteristics.....	52
Table 3.5. Pitch and heave calculated natural periods	55
Table 4.1. Constant values	66
Table 4.2. Added mass coefficients	67
Table 4.3. Geometric properties from selected Pareto Front individuals	75
Table B.1. Generation 100 Population.....	105

LIST OF FIGURES

Figure 1.1 Orientations and degrees of freedom (Goupee et al., 2014).....	3
Figure 1.2. Rendering of 6-MW Sea Reed (EOLFI, 2018)	4
Figure 1.3. Rendering of Gusto MSC Tri-Floater (Huijs et al., 2014)	4
Figure 1.4. 2-MW WindFloat quayside (Principle, 2014).....	5
Figure 1.5. VoltturnUS 1:8 scale quayside (Dagher et al., 2017).....	6
Figure 1.6. Fukushima Mirai installed (Kurtenbachap, 2013).....	6
Figure 1.7. Fukushima Shimpuu, fabrication complete (Mitsubishi Corporation, 2015).....	7
Figure 1.8. Fukushima Forward Hamakaze (Fukushima Offshore Wind Consortium, 2016a).....	8
Figure 1.9. Statoil Hywind Scotland installation mockup (Equinor, 2018).....	8
Figure 1.10. Deployed Tetraspar (Lauridsen, 2017).....	9
Figure 1.11. GICON-SOF installation mockup (GICON-SOF, 2015).....	10
Figure 1.12. Floatgen installed (Ideol, 2018a).....	11
Figure 1.13. Resulting geometries at 6-MW scale, part 1	13
Figure 1.14. Resulting geometries at 6-MW scale, part 2	14
Figure 1.15. Moonpool water motion during oscillation, calm water in transit (Gaillarde & Cotteleer, 2005)	17
Figure 2.1. 1/100 th -scale model of annular hull floating wind turbine a) in the process of trimming the hull and b) during testing	21
Figure 2.2. Model dimensions	22
Figure 2.3. Basin layout	24
Figure 2.4. Mooring line surge restoring force	25

Figure 2.5. Broadband wave spectrums from a) annular hull and b) DeepCwind model test campaigns	26
Figure 2.6. ANSYS AQWA mesh	27
Figure 2.7. Overtopping during regular wave 4.....	31
Figure 2.8. Low-energy surge position RAO magnitude comparison	32
Figure 2.9. Low-energy heave position RAO magnitude comparison	33
Figure 2.10. Low-energy pitch position RAO magnitude comparison.....	33
Figure 2.11. High-energy surge position RAO magnitude comparison	36
Figure 2.12. High-energy heave position RAO magnitude comparison.....	36
Figure 2.13. High-energy pitch position RAO magnitude comparison	37
Figure 2.14. Low-energy nacelle surge acceleration RAO magnitude comparison	39
Figure 2.15. Low-energy nacelle heave acceleration RAO magnitude comparison.....	39
Figure 2.16. High-energy nacelle surge acceleration RAO magnitude comparison.....	41
Figure 2.17. High-energy nacelle heave acceleration RAO magnitude comparison	41
Figure 2.18. ANSYS AQWA heave plate study: Heave RAO magnitude	43
Figure 2.19. ANSYS AQWA heave plate study: Pitch RAO magnitude	43
Figure 3.1. Standardized parameter visual.....	49
Figure 3.2. Resulting footprints	50
Figure 3.3. Square annular hull with wave directions	52
Figure 3.4. Shape variation surge added mass	56
Figure 3.5. Shape variation heave added mass	57
Figure 3.6. Shape variation pitch added inertias	58
Figure 3.7. Shape variation surge RAOs	58

Figure 3.8. Shape variation heave RAOs.....	60
Figure 3.9. Shape variation pitch RAOs.....	61
Figure 4.1. Top-down and section view of hull.....	65
Figure 4.2. NSGA-II Generation 1.....	72
Figure 4.3. NSGA-II Generation 10 and Generation 50.....	73
Figure 4.4. NSGA-II Generation 100.....	74

LIST OF NOMENCLATURE

b	=	moonpool width
c	=	applied damping
c_{cr}	=	critical damping
d	=	draft
f_1	=	mass ratio
f_2	=	pitch natural frequency ratio
g	=	gravitational constant
$\iint x^2 dA$	=	area moment of inertia
I_{pitch}	=	mass moment of inertia of system in pitch degree of freedom
$I_{pitch\ added}$	=	mass moment of inertia of added mass in pitch degree of freedom
K_i	=	waterplane stiffness for i^{th} degree of freedom
$K_{pitch\ hydro}$	=	waterplane stiffness in pitch degree of freedom
$K_{pitch\ mooring}$	=	mooring stiffness in pitch degree of freedom
l	=	length of moonpool
$m_{heave\ added}$	=	added mass in heave degree of freedom
m_{nom}	=	nominal system mass
m_{tot}	=	total system mass
$m_{RNA\ original}$	=	mass of original rotor-nacelle assembly

$m_{RNA\ 6MW}$	=	mass of 6MW rotor-nacelle assembly
$\omega_{pitch\ nom}$	=	nominal pitch natural frequency
P_1	=	moonpool width
P_2	=	hull width
P_3	=	heave plate width
P_4	=	hull height
t	=	hull thickness
θ_{pitch}	=	rotation in pitch degree of freedom
$t_{nominal}$	=	nominal hull thickness
T_{npitch}	=	system pitch natural period
$T_{npiston}$	=	moonpool piston natural period
$T_{nsloshing}$	=	moonpool sloshing natural period
V	=	submerged volume
z_b	=	vertical distance from waterline to center of buoyancy
z_g	=	vertical distance from waterline to center of gravity
ζ	=	damping ratio

LIST OF ACRONYMS AND ABBREVIATIONS

AQWA	=	ANSYS AQWA
DOF	=	degrees of freedom
DNV	=	Det Norske Veritas
FOWT	=	floating offshore wind turbine
GA	=	genetic algorithm
GWh	=	gigawatt hour
kg	=	kilogram
km	=	kilometer
kN	=	kilonewton
m	=	meter
MWL	=	mean waterline
MW	=	megawatt
MWh	=	megawatt hour
NSGA-II	=	Non-dominated Sorting Genetic Algorithm-II
RNA	=	rotor-nacelle assembly
RAO	=	response amplitude operator
s	=	second
TLP	=	tension leg platform

CHAPTER 1

INTRODUCTION

1.1. Motivation

Floating offshore wind turbine (FOWT) hull technologies are evolving rapidly with many technically viable designs. However, a commercially dominant architecture has yet to emerge. Early hull designs including semisubmersible, spar, and tension leg platforms (TLPs) were largely derived from offshore oil technologies but recent developments in the commercial application and optimization of FOWTs have resulted in a number of variations on these three varieties. The appeal of FOWT technology has grown as projects such as Hywind Scotland and the University of Maine's VoltturnUS have seen success and sustainable energy sources have become more desirable. FOWTs also present noteworthy advantages over land and bottom-fixed turbines as they have significant flexibility in where they can be placed and have a high potential to experience consistent winds (Liu et al., 2016; Musial, 2018; Sclavounos, 2008). One example of this is the United States where there is a large concentration of areas off the northeast and west coasts with average wind speeds greater than 8 m/s (WINDEXchange, 2017). In addition to this, much of this wind is more economically accessible by FOWTs as a majority of the offshore wind resources of the United States lies off the coasts of California and New England in waters deeper than 60 m (Manzanas Ochagavia et al., 2013; Musial et al., 2016).

Despite recent successes, resistance to FOWT projects continue largely due to prohibitive cost. Costs for FOWTs are frequently driven by extensive electrical infrastructure and the ocean conditions that must be accounted for in the support system

as compared to land-based systems. Per a 2017 report by Stehly et al., an average land-based system cost \$47/MWh as compared to \$124/MWh for fixed-bottom wind. A floating hull is required to use its geometry as well as an extensive mooring system to minimize turbine motions without being directly rooted to the seafloor. As a result, the per megawatt hour expenditures are even larger than for a fixed-bottom scenario totaling an average of \$146/MWh for FOWT systems (Stehly et al., 2017). Although the cost of technology tends to decrease over time, there is still a significant cost associated with the wind industry.

Unlike land-based wind turbines where foundations are responsible for a mere 4.0% of the project budget, the substructure and foundation for a floating system requires 29.5% of the budget (Stehly et al., 2017). Based on this it is easy to see at least one opportunity for significant savings potential lies in optimizing the geometry of the hull. Reduction in hull size and geometric complexity coupled with increased ease of installation will play a pivotal role in helping the FOWT industry gain forward momentum.

1.2. Background

There are a number of proposed and in-the-works designs for FOWT hulls, each with the goal of surviving the marine environment while also managing to effectively harvest wind energy. In an effort to understand the variety of concepts conceived to date, a wide net was cast investigating commercially viable technologies. Each of the hull technologies detailed in the following sections has its own methods for minimizing platform and turbine motions in the heave, pitch, and surge degrees of freedom (DOF) as

illustrated in Figure 1.1, ranging from the deep drafts of spars to significant buoyancy of semi-submersibles to large magnitudes of mooring tension for TLPs.

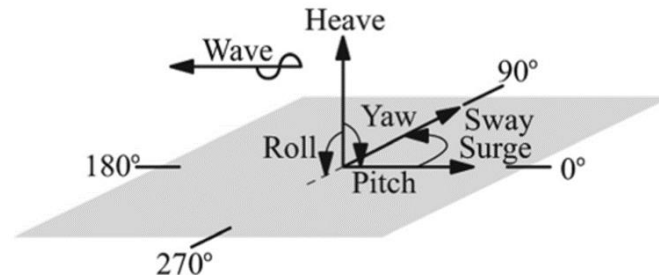


Figure 1.1 Orientations and degrees of freedom (Goupee et al., 2014)

Other hybrid concepts utilize combinations of these characteristics to achieve platform stability. All of the numerous variations that have been developed aim to create a hull which maximizes wind power harnessing potential by minimizing wind turbine motions while keeping cost and other factors in mind. There is a wide variety of existing technologies, but at the end of the exploratory phase, one promising design will be selected for further testing and analysis in the remainder of this thesis.

1.2.1. Existing and in-the-Works Floating Offshore Wind Turbines

The DCNS Sea Reed (Figure 1.2) is a semi-submersible floater that is the result of a collaborative effort between Alstom (now part of GE) and DCNS Marine Energy (now Naval Energies). The Sea Reed hull is designed to support a 6-MW turbine with a hub height (from the waterline to the nacelle) of approximately 100 m and a floater height (from the bottom of the floater to base of the turbine tower) of 35 m. The design was approved by the Bureau Veritas in June of 2017 and installation of four of these hulls is intended to take place part way between Groix and Belle-Ile off the north-western coast of France in 2020 (EOLFI, 2018).



Figure 1.2. Rendering of 6-MW Sea Reed (EOLFI, 2018)

Another triangular semi-submersible concept comes from Gusto MSC. The Gusto MSC Tri-Floater is designed to support a 5-MW turbine at a hub height of 90 m with a draft of 13.2 m (Huijs et al., 2014). The base of each of the three pillars features a heave plate around the perimeter in an attempt to mitigate certain platform motions. The mooring lines are mounted high above the mean water line (MWL) to reduce the overturning moment which is caused by the interaction with the wind; this arrangement is said to permit the use of a smaller floater. Unlike some other floaters, the Tri-Floater does not rely on any active ballasting (GustoMSC, 2019).



Figure 1.3. Rendering of Gusto MSC Tri-Floater (Huijs et al., 2014)

Principle Power's offshore turbine WindFloat (Figure 1.4) also uses a triangular configuration. In this case, the connections between the columns are cylindrical members

which form a truss-like structure. Each of the vertical columns has a heave plate at the bottom. This semi-submersible steel design was used for a 2-MW turbine located off the coast of Portugal which produced over 17GWh of power in a test from 2011-2016. Three 8-MW iterations of this technology are intended to be deployed off the coast of Portugal with funding granted in 2018 (Energias de Portugal, 2018). The WindFloat hull is also intended to be used in a number of other projects globally in the coming years.



Figure 1.4. 2-MW WindFloat quayside (Principle, 2014)

An additional floater in the semisubmersible category is the 1:8 scale VoltornUS floater which was deployed off Castine, Maine for 18 months starting in June of 2013. This floater is a triangular semi-submersible. The floater supports a 12-kW wind turbine. At 1:8 scale, the hull has a draft of 2.9 m and a hub height of 12.2 m. The test site featured a water depth of 15 to 27 m. At full scale, this project is intended to support a 6-MW turbine at a water depth of approximately 100 m (Dagher et al., 2017).



Figure 1.5. VoltturnUS 1:8 scale quayside (Dagher et al., 2017)

Following the Fukushima nuclear disaster of 2011 Japan set out to explore alternative energy sources. As a result of this exploration Japan pursued the potential of floating offshore wind with three FOWT hull designs as part of the Fukushima Forward project. Mirai, the four-column semi-submersible of this project is made from advanced steel and supports a 2-MW downwind wind turbine. It is moored at a depth of 200 m. This hull has a triangular configuration consisting of four columns with the central column supporting the turbine. An active ballast system helps to minimize the floater motions (Fukushima Offshore Wind Consortium, 2013). Funding for the project is provided by Japan's Ministry of Economy, Trade and Industry (offshoreWIND.biz, 2016a).



Figure 1.6. Fukushima Mirai installed (Kurtenbachap, 2013)

Another installment of the Fukushima Forward project is the Fukushima Forward Shimpuu, a V-shaped semi-submersible which supports a 7-MW turbine and is installed at a depth of 200 m. (Fukushima Offshore Wind Consortium, 2016b). The turbine blades alone are 80 m long. Although both the Mirai and Shimpuu are semi-submersible floaters, they have two very different designs. Unlike the Mirai floater, the Shimpuu floater has only three columns and the turbine is mounted on one of the corners of the triangle, rather than in the center. The Shimpuu floater also does not have a complex bracing structure and is built from rectangular prisms instead of cylindrical members.



Figure 1.7. Fukushima Shimpuu, fabrication complete (Mitsubishi Corporation, 2015)

The final FOWT in the Fukushima Forward project's Hamakaze (Figure 1.8). Hamakaze was built as an advanced spar for a 5-MW wind turbine. A traditional spar extends deep below the water's surface, but this concept utilized two hexagonal platforms to attempt to achieve the goal of ballast stabilization with a smaller draft. Unfortunately, this hull was met with great difficulty in the installation process as the platform tilted so far to one side that it took days to right it (offshoreWIND.biz, 2016b). Similar to the

other two FOWTs in the project, Hamakaze was moored at a depth of approximately 200 m (Fukushima Offshore Wind Consortium, 2013).



Figure 1.8. Fukushima Forward Hamakaze (Fukushima Offshore Wind Consortium, 2016a)

Statoil's Hywind Scotland (Figure 1.9) takes a more traditional approach to the spar with a cylindrical hull featuring a deep draft to utilize the stabilization from the low center of gravity provided by the ballast. After testing a near commercial-scale prototype with a 2.3-MW turbine off the coast of Norway—which saw winds of up to 40 m/s and a maximum wave height of 19 m—a demonstration farm with full-scale turbines was deployed in Scotland and started providing power to the grid in October of 2017. The full scale deployment features five 6-MW turbines moored at water depths of 95 to 129 m and is the world's first floating wind farms (Equinor, 2018).



Figure 1.9. Statoil Hywind Scotland installation mockup (Equinor, 2018)

The concept of Tetraspur was released in 2015 by Henrik Stiesdal. Unlike the preceding hulls, the details of Tetraspur were fully released to the public. The intent of

this release was to enable any interested parties to push the development of this idea forward. Tetraspar was designed to be a low-cost system with easy tow out and the ability to be installed in water depths ranging from 10 m to 1000 m (Dvorak, 2015). The original concept utilizes air-filled canisters at the bottom of the hull to provide flotation. The Tetraspar can be deployed as a TLP with an anchor or a spar with a hanging mass as shown in Figure 1.10.



Figure 1.10. Deployed Tetraspar (Lauridsen, 2017)

One example of a more traditional approach to the TLP is the TLP utilized by GICON-SOF. As is typical of a TLP, the GICON-SOF is moored with taught vertical mooring lines. The lines are attached to a large mass that sits on the sea floor as shown in Figure 1.11. In this case, the hull is made from high performance prestressed concrete and is intended to float out on top of a barge. The purpose of the barge is two-fold as it is intended to be ballasted once it arrives at the installation site and lowered from the keel to be used as the anchor for the system (GICON-SOF, 2018). The GICON-SOF concept is still in development, but has been tested at a 1/37th scale in wind and waves at Maritime

Research Institute Netherlands. Supporting a 2.3-MW turbine would require that the outer footprint of the floater measure 32 m by 32 m (Großmann et al., 2014).



Figure 1.11. GICON-SOF installation mockup (GICON-SOF, 2015)

The Ideol floating foundation does not resemble any of the aforementioned oil and gas-style floating foundation examples. This hull is somewhat of a combination of a barge and a typical semi-submersible hull. The item of greatest interest in this design is the use of a moonpool (a material void) which is centrally located on the waterplane area. The intended purpose of the moonpool is to use the water within it to counteract the motion of the waters on the exterior of the hull. The hull geometry enables simpler construction techniques and the low draft permits quayside turbine erection in a large number of ports, eliminating costly turbine erection operations at sea. In addition, the annular hull arrangement is stable during tow-out and only requires low-cost vessels for installation.

A 2-MW version of this design has been deployed in France and was commissioned in 2018 (Ideol, 2018c). The assembly is located approximately 22 km

from shore where the depth of the water is roughly 33 m. The maximum height of the waves at this location is 16 m (Greenovate! Europe EEIG, 2013). A 3-MW iteration deployed in Japan has been also been installed since 2018 (Ideol, 2018b). The success of these installations inspire some confidence in the design and demonstrate significant potential for scalability of the technology.



Figure 1.12. Floatgen installed (Ideol, 2018a)

1.2.2. Use of Froude Scaling to Derive Equivalent 6-MW Systems

To facilitate better comparisons of the various designs in the previous section, the FOWTs were resized such that they all supported a similar, 6-MW commercial-scale wind turbine. To begin this process, the approximate dimensions for each system were obtained based on published information and/or derived using known information along with images of the systems. Due to the approximate nature of this process it is noted that the results are not without at least some error. The next step in the process was to scale each model to be able to support a 6-MW turbine. Although there are a variety of turbine sizes in floating offshore wind, a 6-MW turbine represents a well-developed design space that is both realistic and attainable (the Hywind project discussed previously consists of

five turbines of this size). The turbine was assumed to be installed at a hub height of 100 m with a rotor diameter of 150 m. The process of scaling these hulls was completed using Froude Scaling (Chakrabarti, 1994). The scaling factor, λ , employed in the Froude scaling process was calculated by taking the cube root of the ratio of the mass of the rotor nacelle assembly (RNA) for the baseline turbine for each system as compared to the RNA of a standard 6-MW wind turbine as illustrated in (1.1).

$$\lambda^3 = \frac{m_{RNA\ original}}{m_{RNA\ 6MW}} = \frac{m_{RNA\ original}}{450t} \quad (1.1)$$

Where: $m_{RNA\ original}$ is the mass of the original RNA
 $m_{RNA\ 6MW}$ is the mass of the 6-MW RNA

Relevant scale factor information is provided in Table 1.1. The original turbine sizes and scaling factor for each hull are specified in Table 1.2. Resulting geometries for the support of 6-MW turbines are shown in Figure 1.13 and Figure 1.14.

Table 1.1. Wind turbine scaling guidelines

Parameter	Scale Factor
Length	λ
Volume	λ^3
Mass	λ^3

Table 1.2. 6-MW Froude Scaling information

FOWT Name	Baseline Turbine Size (MW)	Baseline Turbine Mass (mt)	Scale Factor
DCNS Sea Reed	6	450	1.000
Fukushima Forward Mirai	2	100	1.615
GustoMSC Tri-Floater	5	350	1.078
Principle Power WindFloat	2	100	1.615
GICON-SOF	2.3	150	1.456
Fukushima Forward Shimpuu	7	500	0.960
Ideol	2	100	1.546
Fukushima Forward Hamakaze	5	350	1.078
Statoil Hywind	6	350	1.068
Tetraspar	6	450	1.000
VolturnUS	6	450	1.000

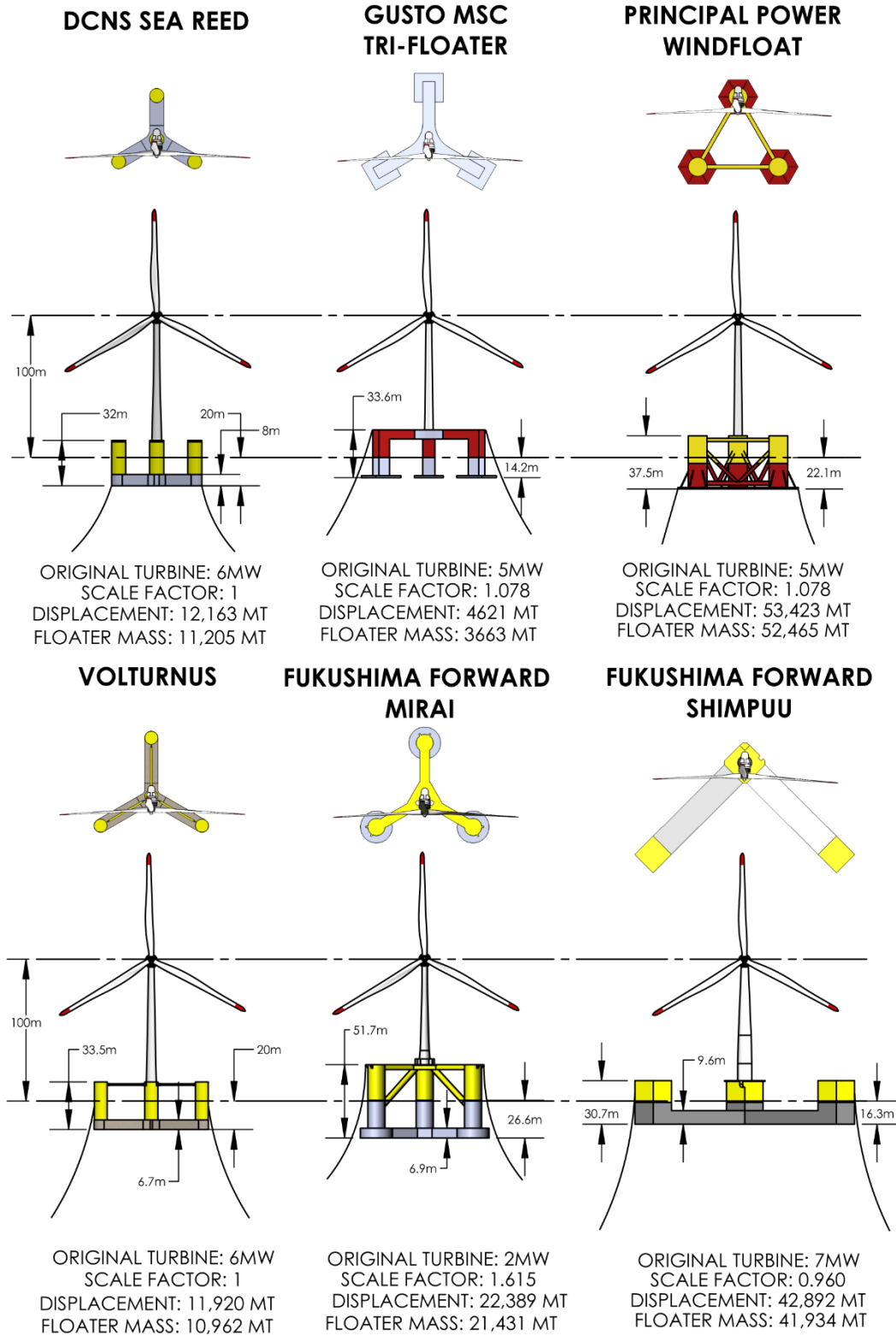


Figure 1.13. Resulting geometries at 6-MW scale, part 1

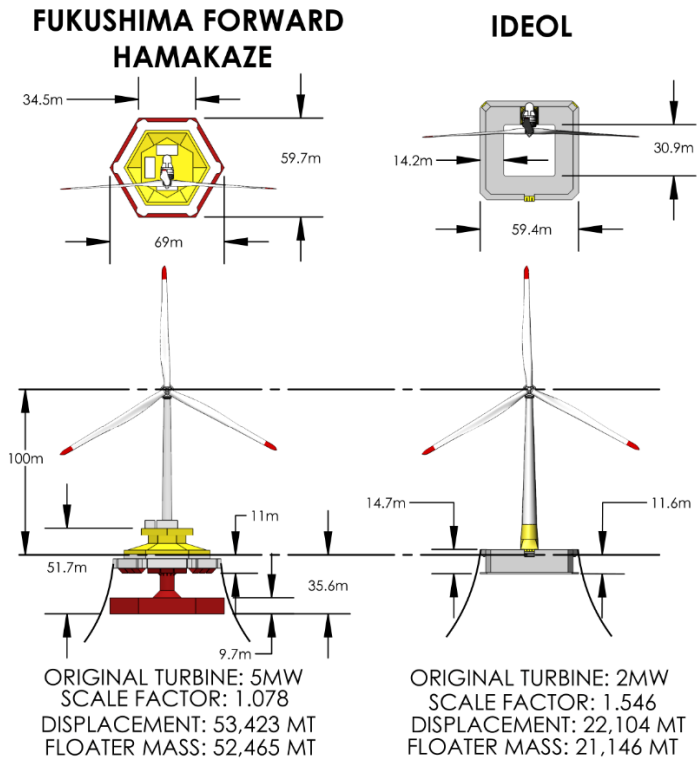
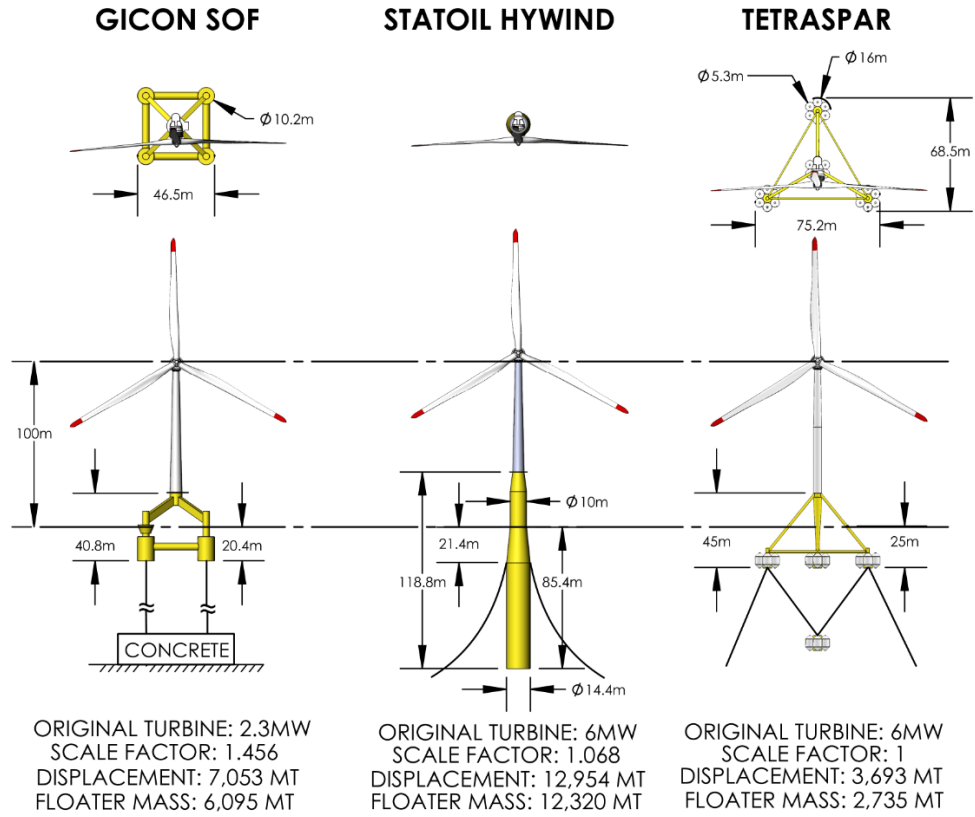


Figure 1.14. Resulting geometries at 6-MW scale, part 2

With each hull scaled to support a 6-MW wind turbine the geometries of the systems were compared. Specific attention was paid to the footprint, draft, and any unique qualities. A significant majority of the systems reviewed are semisubmersible tri-floaters. Although this seems to indicate the significant potential for success of this category, it also does not leave very much room for variability. The Hamakaze hull exhibited significant issues in installation and a more traditional spar does not allow for flexibility for affordable quayside turbine installation. Considering these factors as well as the scarcity of publicly available global performance test data for floating hulls with large moonpools relative to the size of the hull, the Ideol model was selected for further studies. In order to best quantify the potential of such a design, there is significant interest in understanding the dynamic performance of the moonpool of this hull and how it impacts the system motions through both experimental and computational means.

1.2.3. Moonpools

The main focus of this thesis is on the data generation, model validation, and optimization of a hull with a moonpool that is capable of supporting a 6-MW turbine. A moonpool is a material void (shaft) which allows for water movement under and/or within a hull or other floating body. Moonpools are widely used as a method of accessing the subsea area with reduced impacts from exterior horizontal and vertical water motions (Gaillard & Cotteleer, 2005). The damping benefits involved in the applications of moonpools are considered in three parts: potential/radiation damping, friction damping, and viscous damping. The radiation damping is provided by outgoing waves that are the result of the motion of the body and it is considered relatively small. There is some damping which results from the friction of the water moving along the inner surface of

the moonpool, but this damping is considered to be negligible (Aalbers, 1984). This leaves the viscous pressure damping as the most impactful form of damping resulting from the moonpool.

Viscous damping is caused by vortex shedding due to vertical piston motion within the moonpool which starts as the motion of the water in the moonpool nears its piston natural frequency (see (1.2)) (Gaillarde & Cotteleer, 2005). As the water within the moonpool moves in the vertical direction, the downward motion of the water coupled with the sharp edges at the base of the moonpool causes vortices to shed and a downward forcing on the hull results in an increase in heave damping (Aalbers, 1984; Beyer et al., 2015).

$$T_{n \text{ piston}} = 2\pi \sqrt{\frac{d + 0.41\sqrt{bl}}{g}} \quad (1.2)$$

Where: d is the draft of the hull

b is the width of the moonpool*

l is the length of the moonpool*

g is the gravitational constant

*the product of bl was approximated as the surface area of the pool for the triangular and circular hulls discussed later

While the piston motion inside the moonpool represents the vertical motion of the water, sloshing describes the primarily horizontal motion within the moonpool which is caused by surge and sway motion from the structure. In the case of a moonpool in transit in calm water illustrated in Figure 1.15, the sloshing motion occurs at the surface of the moonpool, starting at one edge of the pool and moving to the opposite edge.

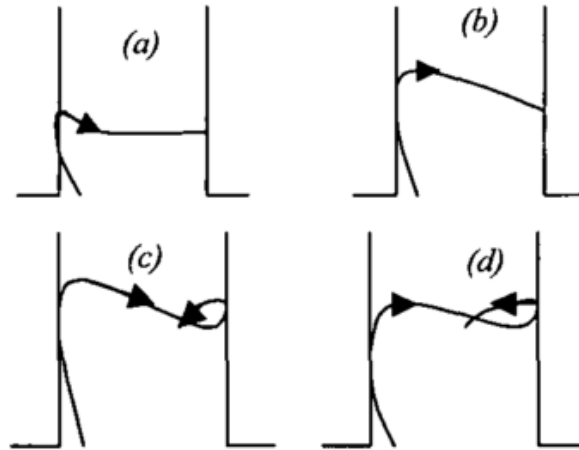


Figure 1.15. Moonpool water motion during oscillation, calm water in transit (Gaillarde & Cotteleer, 2005)

As the motion begins to reflect back from the right edge of the moonpool to the starting edge as shown in part c, the new wave that is forming on the left and moving to the right begins to move to the right. When these two waves meet, there is a cancelling effect in the motion of the water (Gaillarde & Cotteleer, 2005). This motion is initiated by water motions outside the pool, but it also serves to at least partially counteract them. When it comes to the offshore environment this represents a simplified case as there would be waves coming from multiple directions with varying frequencies, but the principles are likely to be very similar. The sloshing motion in a moonpool most prominent at the sloshing natural period according to (1.3) (Molin, 2001).

$$T_{n_{sloshing}} = 2\pi \sqrt{g \frac{\pi}{b} \coth \left(\frac{\pi d}{b} + 1.030 \right)} \quad (1.3)$$

Where: g is the gravitational constant
 b is the width of the moonpool
 d is the draft of the hull

1.3. Research Contributions

The following academic contributions made by this thesis are as follows:

- A review of experimental and numerical modeling methodologies including modeling parameters and response amplitude operator (RAO) results to enable replication of testing.
- Capturing the impacts of moonpools on FOWT global performance in numerical modeling including tuning of lid characteristics.
- Assessment of FOWT global performance impacts resulting from moonpool shape variation.
- A study of quantifying the geometric tradeoffs of annular hulls when optimizing mass and pitch natural frequency

1.4. Thesis Overview

Chapter 2 will describe the scale model testing parameters and the application of Froude scaling to size the selected hull to model scale. Following this, the numerical model validation process will be described. This description will include mesh and other settings utilized in ANSYS AQWA (AQWA). AQWA is a hydrodynamic software that uses a panel code to generate a potential flow solution to facilitate analysis in the time domain as well as the frequency domain (ANSYS Inc., 2013a). For the purposes of this work the Hydrodynamic Diffraction and Hydrodynamic Response analysis systems were used to generate results in the frequency domain utilizing only the geometry at or below the mean water line. Results comparisons between the scaled experimental model and numerical model will also be reviewed.

In Chapter 3 numerical models of three alternative annular hull geometries will be compared along with one barge model. Specified properties will be held constant across all geometries while the dimensions of the waterplane area of the hulls will be permitted to vary. The alternative geometries will be quantitatively evaluated for their linear static stability, added mass/inertia and natural frequencies in surge, heave, and pitch DOF. In addition, other factors such as cost will be discussed.

The contents of Chapter 4 revolve around the optimization of the hull geometry selected in Chapter 3. The optimization process will explore the range of designs that result from optimizing hull performance in platform pitch motion and system mass simultaneously. While these features are optimized the draft, outer perimeter, and other properties are permitted to vary. Unlike the hull resulting from Chapter 3 the optimized hull is permitted to feature heave plates as an additional variation.

Conclusions and future work will be covered in Chapter 5. Final thoughts on the numerical modeling process in regards to recommendations for and a review of methods for appropriately modeling moored models with moonpools will be provided. The geometric comparison results will then be revisited including a review of considered parameters. Optimization of the square annular hull will also be discussed in Chapter 5. The chapter will close with a discussion of areas which are recommended for further investigation.

CHAPTER 2

EXPERIMENTAL COMPARISON OF AN ANNULAR FLOATING OFFSHORE WIND TURBINE HULL AGAINST PAST MODEL TEST DATA

2.1. Introduction

With the annular 6-MW system selected, this chapter takes a closer look at the performance of the system at model scale and attempts to reproduce those results with numerical modeling. Although the intent of this study is to determine how an annular hull-based system could behave, it is important to note that the system herein is considered a generic system and is similar but not an exact reproduction of other annular hulls proposed by Ideol and others.

Experimental modeling was completed for a generic 6-MW annular hull FOWT at 1/100th-scale in the University of Maine's Harold Alford Wind Wave (W2) Ocean Engineering Laboratory in 2018. Although testing was carried out at model scale, all data reported in this chapter is presented at full scale. The hydrodynamic performance of the same FOWT was also modeled using AQWA. Comparison of experimental and simulation RAO magnitudes for key positions and accelerations are conducted in an effort to validate the AQWA simulations. RAO magnitudes represent the normalized motion response of the system per unit wave amplitude input for a given wave frequency. The experimental and simulation results for the annular FOWT hull are also compared to a large model test data set obtained for the 5-MW DeepCwind semisubmersible, spar and TLP for the purposes of putting the annular hull hydrodynamic performance in context (Goupee et al., 2014; Koo et al., 2014). This past publically available data set has been used extensively for numerical validation and represents reasonable performance of the traditional floating hull design types (Hermans et al., 2016; Robertson & Jonkman, 2011).

2.2. Model Description

Both the experimental and numerical modeling completed considers a hull sized to support a 6-MW turbine with a hub height of 100 m above the MWL. The models used an equivalent point mass in place of a turbine and take only wave forcing into account. Prior results (e.g. see (Goupee et al., 2014)) have shown that the linear wave response of a FOWT's dynamics are only weakly influenced by wind turbine forcing in the range of periods considered, and as such, it is neglected here for simplicity (Coulling et al., 2013). That noted, the annular hull geometry considered is generic with a square outer perimeter and moonpool opening, as shown in Figure 2.1.

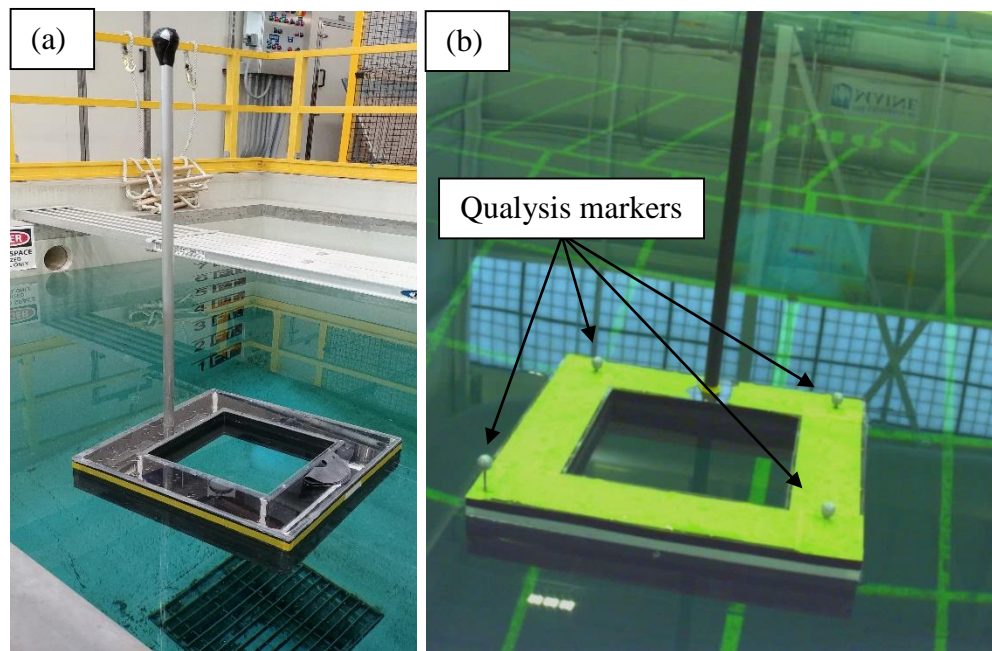


Figure 2.1. 1/100th-scale model of annular hull floating wind turbine a) in the process of trimming the hull and b) during testing

All dimensions were approximated for a 2-MW system based on publicly available data (LHEEA Centrale Nantes, 2018) and scaled to accommodate a 6-MW turbine using Froude scaling (Det Norske Veritas, 2014). The Froude scaling was

completed based on the scale factor resulting from the cube root of the ratio of the mass of the 6-MW turbine as compared to the mass of the 2-MW turbine. The scale factor obtained was 1.546. With the exception of the hub height, each length dimension from the 2-MW system was scaled to the 6-MW system by multiplying the dimension by the scaling factor. Additional system properties were calculated using the scaling factor and Froude-scaling rules accordingly. The geometry of the tested annular hull, including the local coordinate system used in this work, is given in Figure 2.2.

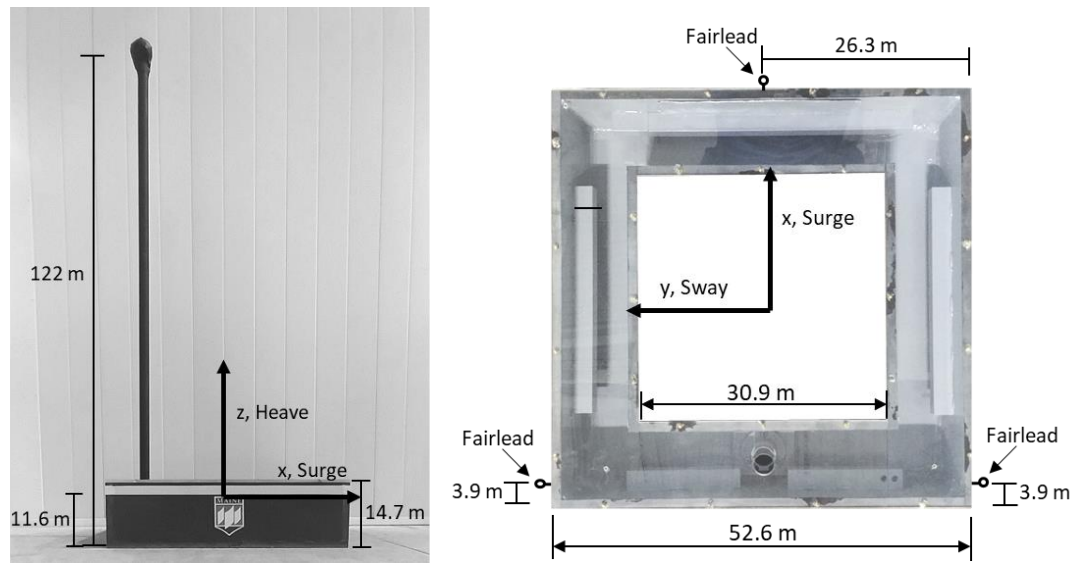


Figure 2.2. Model dimensions

The resulting gross properties of the 6-MW-sized hull are given in Table 2.1. Surge, heave and pitch natural periods specified are obtained from free-decay testing. In the case of heave, two harmonics were observed in the free-decay results with similar periods, with the stronger of the two being 8.1 s. The weaker value harmonic exhibited a period of approximately 10 s. The heave free-decay test results indicate a significant coupling between the moonpool piston natural period and the heave natural period. Calculations for the heave natural period of the system yield an expected value of 10.1 s.

Table 2.1. Select model specifications

Specification (units)	Specified Value	As-Built	% Difference
Total System Mass (mt)	21,341	20,880	2.18
Displacement (mt)	21,479	21,019	2.16
Draft (m)	11.6	11.6	0.0
Center of Gravity Above Keel (m)	10.5	10.6	0.95
Hub Height (m)	100	105.7	5.54
Roll Inertia (kgm ²)	1.149×10^{10}	1.480×10^{10}	25.18
Pitch Inertia (kgm ²)	1.149×10^{10}	1.609×10^{10}	33.36
Yaw Inertia (kgm ²)	1.859×10^{10}	1.859×10^{10}	0
Surge Natural Period (s)	--‡	121.4	--
Heave Natural Period (s)	10.1	8.1*	21.98
Pitch Natural Period (s)	11.6	12.2	5.04
Moonpool sloshing natural period (s) §	6.35	--	--

*Secondary harmonic observed at roughly 10 seconds

‡ Dependent on mooring characteristics

§As calculated from (Molin, 2001)

Geometric differences between the model considered here and the similar concept produced by Ideol and currently deployed off the coast of France are that the system considered here exhibits an absence of heave plates and corner chamfering. The approximately 2 m-wide heave plates of the 2-MW Ideol system run along the base of the outer perimeter of the hull. Each corner on the Ideol hull also features significant chamfering at the outer corners. The scale model of Figure 2.2 was constructed without these geometric complexities, but the simplified geometry used here is expected to adequately capture the general global response behavior of an annular hull system (i.e., similar physical and added mass properties, similar hydrostatics). Discussion of a case study regarding the impacts of the application of heave plates can be found in Section 2.5.3.

During testing three mooring lines were attached to the hull at the MWL; one at the bow and one at the aft portion of port and starboard sides. The layout of the mooring

system is given in Figure 2.3. With the coordinate system in Figure 2.2 showing the origin centered at the intersection the hull's water plane area centroid and at the MWL, the bow, port and starboard anchors were located at (7.57 m, 0 m, 0 m), (-2.18 m, 4.5 m, 0 m) and (-2.18 m, -4.5 m, 0 m), respectively. The mooring lines were designed to prevent significant drift of the model, but also to be soft enough to yield a reasonable surge natural period for a hull of this size as well as not significantly influence the heave and pitch motion of the system. The surge restoring force provided by the complete mooring system as measured in the basin is provided in Figure 2.4.

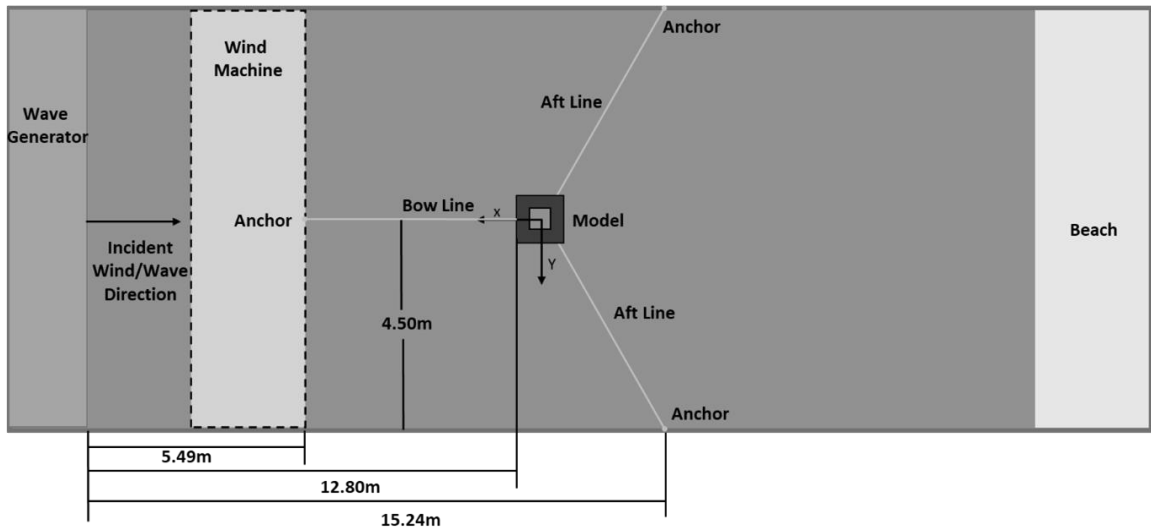


Figure 2.3. Basin layout

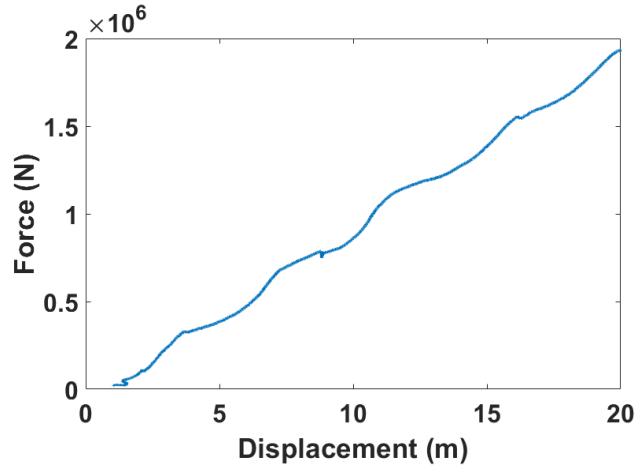


Figure 2.4. Mooring line surge restoring force

2.3. Testing Environments

Testing was completed in the W2 with the water depth set to 4.5 m. Prior to testing the model in any wave environments, free-decay tests were performed to characterize the system. The natural periods obtained from these tests are provided in Table 2.1. Following these tests, the hull was tested in the W2 and subjected to a variety of wave environments including a set of five regular waves as well as two irregular waves with broad band spectrums (a low-energy white noise sea state and a high-energy white noise sea state). The details of the wave environments for both this test campaign and the 2011 DeepCwind model tests are provided in Table 2.2 and Table 2.3, and each of the irregular wave spectrums used are given in Figure 2.5. All hull motion tracking for the annular hull was performed using four Qualisys markers positioned near each corner on the top face of the hull as shown in Figure 2.1.

Table 2.2. Regular wave characteristics

Wave Amplitude (m)	Period (s)
0.99	7.15
3.17	9.3
7.91	13.1
9.95	14.2
11.63	15.0

Table 2.3. Broadband wave characteristics

Hull	Relative Energy Level	Hs (m)	Period Range (s)
Annular	Low	3.33	5-25
	High	8.71	5-25
DeepCwind	Low	6.98	6-26
	High	11.33	6-26

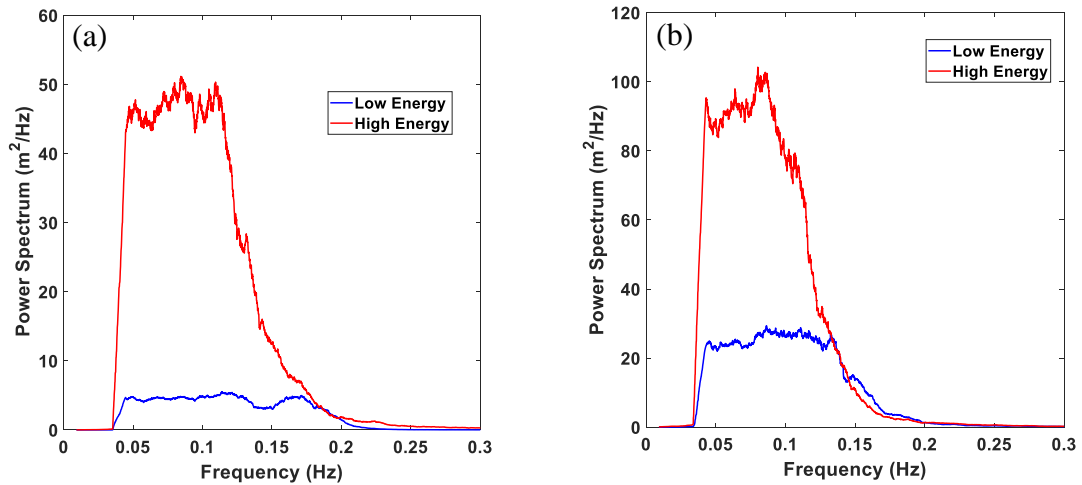


Figure 2.5. Broadband wave spectrums from a) annular hull and b) DeepCwind model test campaigns

2.4. Numerical Modeling

All numerical modeling was executed using ANSYS AQWA Version 19.1 utilizing all of the geometric and mass properties as measured from the experimental model. Similar to the model tests, numerical modeling considered only hydrodynamic loading and excluded wind loading. The entire system was treated as a single rigid body for all simulations.

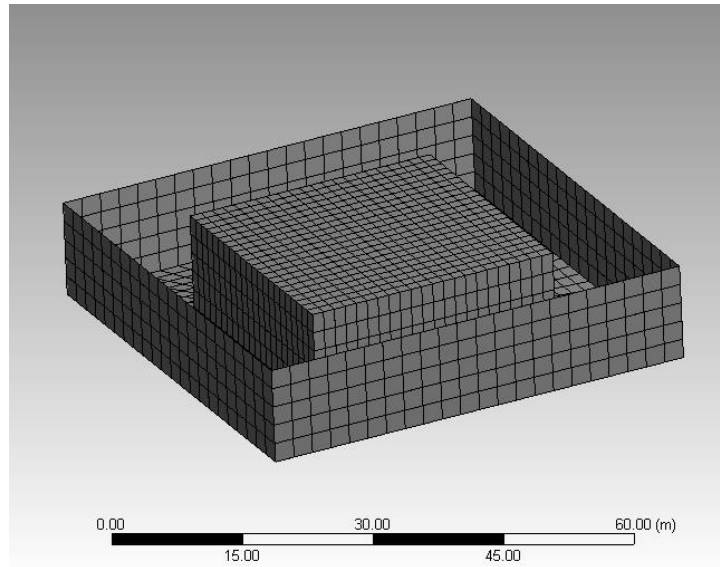


Figure 2.6. ANSYS AQWA mesh

A convergence study was performed comparing three possible meshes: one with a maximum element size of 8.0 m, one with a maximum element size of 4.0 m and the final case with a maximum element size of 1.5 m. Comparing surge, heave and pitch RAO results for these three cases yielded similar response predictions with less than a 1% difference in the maximum RAO values in the wave period range of interest of 5 to 20 s. Based on these results, the mesh with a maximum element size of 4.0 m was chosen which featured 2025 nodes and 1980 total elements (see Figure 2.6). A frequency domain analysis was conducted using this mesh with 90 evenly-spaced wave frequencies ranging from 0.05 Hz to 0.2 Hz. Mooring line interactions from the experimental setup were captured using an additional stiffness term in the surge direction of 94.2 kN/m.

In ANSYS AQWA, an external lid was used to account for the motions of the water within the moonpool geometry. Two parameters are available for customization of external lid properties, the gap and the damping factor. For this study the gap value was set to the width of the moonpool per the AQWA User's Manual (ANSYS Inc., 2013b).

The damping factor for the moonpool required a bit of further exploration as the damping is applied to suppress standing waves within the pool. These standing waves are the result of the computational process and do not necessarily illustrate occurrences during testing or deployment of the structure. The damping factor input ranges between 0 and 1 with 0 providing no damping and 1 damping all vertical surface velocity (ANSYS Inc., 2013b). Determining the ideal lid damping value required an additional study into system behavior in low and high-energy sea states using tank data. The lid damping combines with additional system damping in heave and pitch DOF, both of which must be tailored in order to best replicate experimental results. Further discussion of this investigation follows in the subsequent paragraphs.

Along with the damping applied to the external lid there was also external system linear damping applied in pitch and heave DOF in an attempt to replicate viscous drag not simulated within AQWA. No additional external damping was applied in the surge direction. The lack of additional external damping in surge is due to the fact that viscous damping most strongly impacts resonant motions, and the surge natural period of the system considered here is far outside the range of wave periods investigated in the AQWA frequency domain analysis. The same cannot be said for the resonant heave and pitch motions as the natural periods for both of these DOF lay within the range of interest for the AQWA analyses. As such, external damping is included in the heave and pitch DOF for all AQWA analyses. In addition, the nonlinear nature of the external viscous damping changes significantly with motion amplitude, and therefore, distinct linear values are employed to best replicate the experimental responses observed for the low-energy and high-energy sea state tests.

After a manual calibration phase employing the free-decay test results, the additional pitch linear damping values applied in AQWA for this particular system for low and high-energy wave states were roughly 4% and 13% of critical pitch damping, respectively. Initial simulation results obtained for the heave RAO magnitudes demonstrated sensitivities to the variation of external heave linear damping as well as the damping factor applied to the lid. Based on this finding, these two values were varied manually to obtain a good fit with the overall surge, heave and pitch RAO experimental results as the lid damping influenced not only the heave response, but surge and pitch DOF as well. The results of this study suggest that a heave linear damping of 3% of critical and a lid damping factor of 0.0001 (i.e. negligible) fit best for the low wave energy case and a heave linear damping value of 10% of critical combined with a 0.05 lid damping factor match best with experimental results for the high-energy wave case. The lid damping factor necessary to generate similar responses to the model test results in low-energy wave cases suggests that the lid may not even be necessary. By contrast, the lid damping factor required for high-energy cases indicates that it is highly important in these situations. The values provided are specific to the hull configuration and environments presented herein and do not necessarily correspond to the ideal values for other geometries.

2.5. Results

With the generation of experimental and numerical data complete, the system responses for both cases can be compared. In addition to this comparison, the comparison of the annular system with the results from DeepCwind systems is also detailed in the following sections.

2.5.1. Position RAO Magnitudes

When looking at the behavior of a floating wind turbine, the wave-induced motion of the hull is highly important. For the long-crested waves considered in this work, the hull DOF of particular concern are surge, heave and pitch. The responses in these particular DOF play a large role in characterizing a FOWT's ability to survive the deep ocean environment as well as minimize wind turbine motions to facilitate smooth power production. Platforms that minimize wave-induced motions also diminish fatigue and ultimate loads in the tower, turbine, hull, mooring system and umbilical. To assess the motion performance of the annular hull FOWT subjected to wave loading, the surge, heave and pitch RAO magnitudes from both simulation and experiment are presented and discussed in the subsequent sections.

2.5.1.1. Low-Energy Position RAO Magnitudes

Results from regular wave testing for low-energy waves are shown in Figure 2.8 through Figure 2.10. Shown in Figure 2.8 and Figure 2.9, the irregular wave-derived RAO magnitude trends follow the regular wave trends for surge and heave fairly well. By contrast, significant differences between the regular wave and low-energy RAO magnitudes are found for the 13.1 s and 14.2 s cases for platform pitch. Regular wave testing at 13.1 s and 14.2 s period caused significant green water, yielding appreciable nonlinearity in the platform response and likely causing the discrepancy between the regular and irregular results (e.g. see Figure 2.7). The low-energy white noise wave did not possess significant green water events, and as such, the experimental data displays a typical resonant response much like the linear AQWA simulations.



Figure 2.7. Overtopping during regular wave 4

The AQWA simulation for the low-energy position RAO magnitudes capture the overall trends of the experimental results with reasonable accuracy. One notable difference between these two data sets is in the wave period yielding the peak pitch response. As seen in Figure 2.10, the largest pitch RAO magnitude occurs at a period of 12.8 s experimentally and 13.2 s in the AQWA model. This discrepancy may be due to several factors including uncertainty in the measured system pitch inertia, small differences between the actual and AQWA-calculated added-inertias, and platform pitch stiffness contributions provided by the mooring system which were not included in the simulations. Regarding the peak pitch RAO magnitude of Figure 2.10, the difference between the experimental and AWQA results is only 1.5%.

The surge response for the DeepCwind TLP exhibits similar trends to the annular hull up to a period of approximately 12 s before it departs and maintains a larger magnitude through the remaining periods of interest. By contrast, the DeepCwind spar has a significantly lower surge response across all periods of interest. While results for the annular hull show very similar results to the DeepCwind semisubmersible in surge as

seen in Figure 2.8, the heave responses in the low-energy waves for periods between 5 and 15 s shown in Figure 2.9 are significantly larger for the annular hull system. Heave responses from the DeepCwind TLP and spar are significantly lower than both the semisubmersible and the annular model with magnitudes of less than 0.1 m/m across the periods shown. Despite these differences, the resonant response in heave for the annular hull does not greatly exceed a value of 1 in the range of approximately 10 to 12 s. Referring once again to Figure 2.10, the peak pitch RAO magnitude obtained for the low-energy white noise wave is significantly higher than the magnitude of the peak value observed for all three DeepCwind systems over the wave period range of interest. This is largely due to the fact that the annular hull system exhibits a resonant response at a period of approximately 12 s whereas the DeepCwind hulls do not as their platform pitch natural periods are outside of the wave period range shown in Figure 2.10.

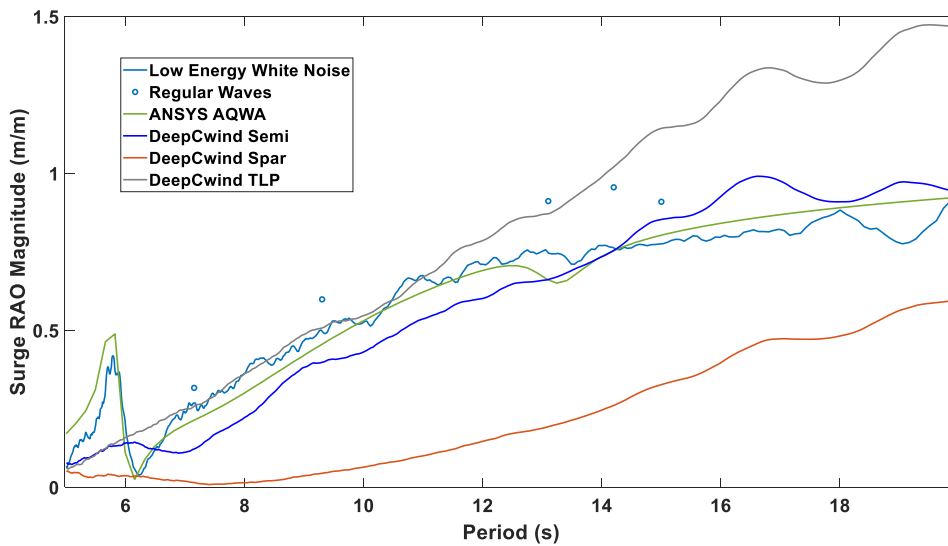


Figure 2.8. Low-energy surge position RAO magnitude comparison

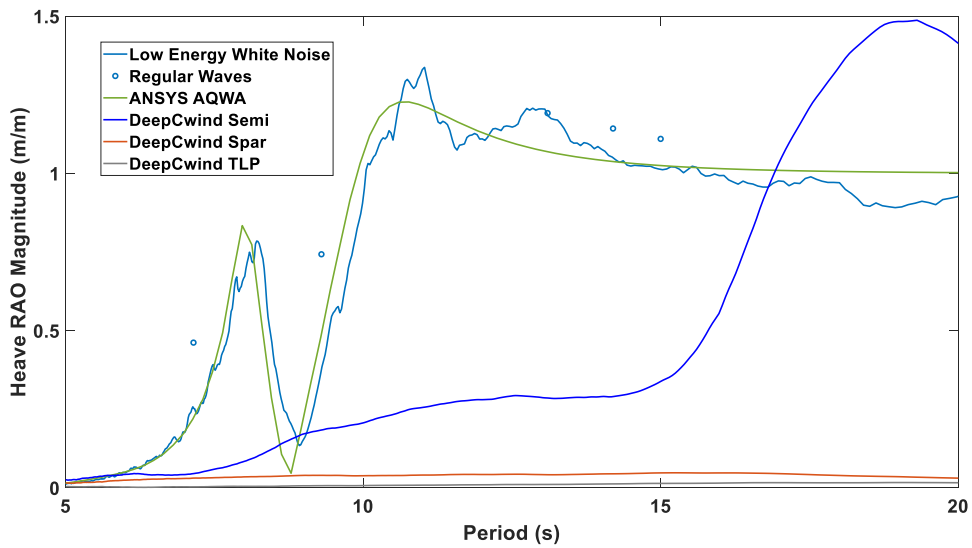


Figure 2.9. Low-energy heave position RAO magnitude comparison

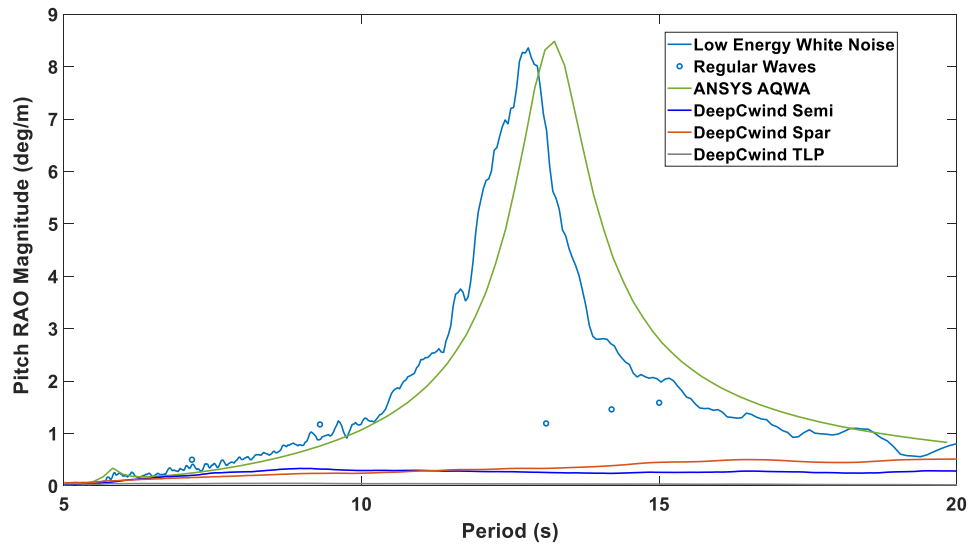


Figure 2.10. Low-energy pitch position RAO magnitude comparison

2.5.1.2. High-Energy Position RAO Magnitudes

The high-energy white noise wave-derived position RAO results are shown in Figure 2.11 through Figure 2.13. As seen in Figure 2.11 and Figure 2.12, the surge and heave RAO magnitudes derived from the high-energy irregular waves are fairly similar to

those for the regular waves, albeit, the comparison is not as good as for the low-energy heave irregular wave results of Figure 2.9. For the platform pitch RAO of Figure 2.13, the high-energy white noise compares well with 3 of the 5 regular wave results, with the two major differences occurring between the two at periods of 13.1 s and 14.2 s. The cause for the discrepancy is the same as that noted for the results of Figure 2.10.

Comparing the low-energy (Figure 2.8 through Figure 2.10) and high-energy (Figure 2.11 through Figure 2.13) white noise wave-obtained RAO magnitudes, several differences can be observed. With increased wave energy, and hence motion amplitude, it is seen that surge RAO response at a period of approximately 6 seconds is diminished, likely as a result of resonance of the horizontal sloshing motion within the moonpool. Additionally, the heave and pitch RAO magnitude peak responses near system resonance are also diminished (see Table 2.1) at periods of roughly 10 and 13 s, respectively. This is expected as viscous damping is proportional to the square of the platform velocity. The increase in hydrodynamic damping for the high-energy sea state most strongly influences resonant responses of the system, hence the observed differences between the two white noise wave test RAO magnitudes.

As seen in Figure 2.11, the AQWA simulations match well with the experimental results in surge. Using an appropriate set of lid and added system damping coefficients in heave, the AQWA results for the heave RAO magnitudes in this high-energy irregular sea state compare well with experimental data throughout the entire period range of interest. The AQWA pitch results demonstrate a slightly higher pitch magnitude with a 3.3% difference between the peak pitch RAO and the experimental results. While a discrepancy exists between the AQWA predictions and experimental peak pitch RAO

response period for the low-energy white noise wave RAO magnitudes, the difference between the periods for the high-energy case of Figure 2.13 is much smaller.

Comparing the annular hull and DeepCwind semisubmersible, the two systems once again exhibit similar surge RAO trends as shown in Figure 2.11. The surge performance of the spar and TLP as relative to the annular hull system is also very similar to that found in the low-energy case. Observing the high-energy wave heave RAO magnitudes (Figure 2.12), it can be seen that the annular hull system possesses significantly greater heave motion for wave periods in the 10 to 15 s range, with the DeepCwind semisubmersible exhibiting a greater response for periods of approximately 17 s or larger, this being a period typically outside the peak period of most design sea-states. The spar and TLP both have lower surge RAO magnitudes than both the semisubmersible and the annular hull from the period of about 6 s through to the 20 s period. Similar to the low-energy wave case, the high-energy case for platform pitch shows a significant difference between the DeepCwind semisubmersible and the annular hull system RAO magnitudes with the maximum value of the annular system approximately seven times that of the DeepCwind system. The DeepCwind spar exhibits similar pitch performance to the semisubmersible. The platform pitch RAO magnitude of the TLP is very small, as one would expect, and is less than 0.1 deg/m throughout the range of periods shown.

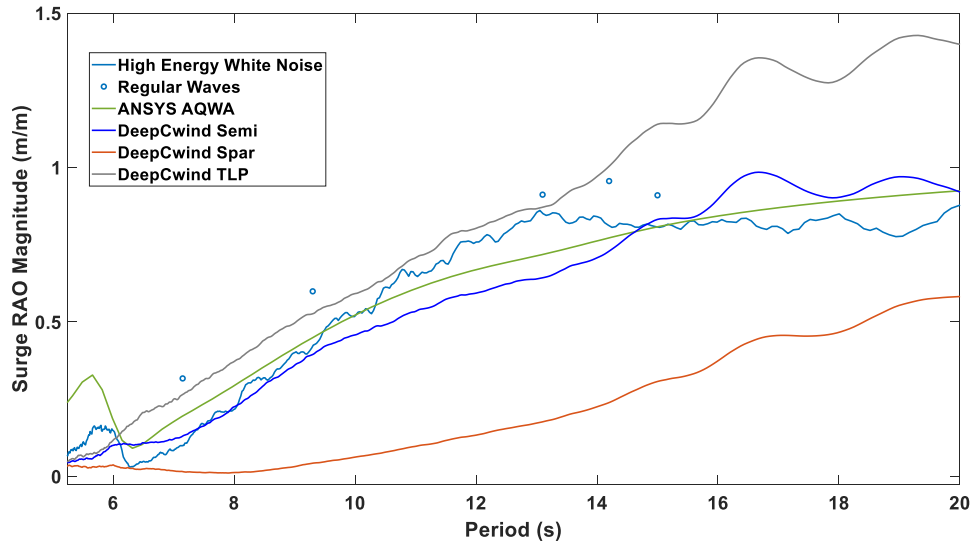


Figure 2.11. High-energy surge position RAO magnitude comparison

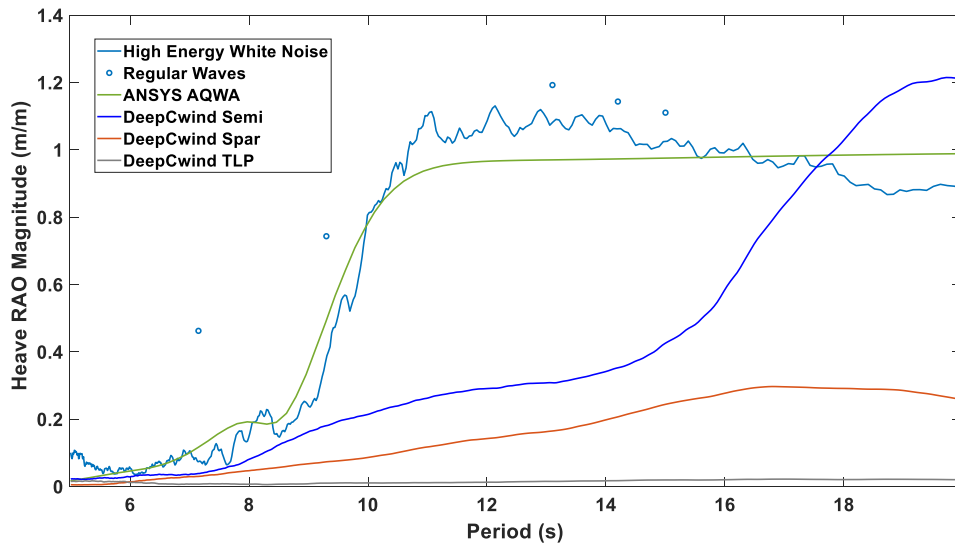


Figure 2.12. High-energy heave position RAO magnitude comparison

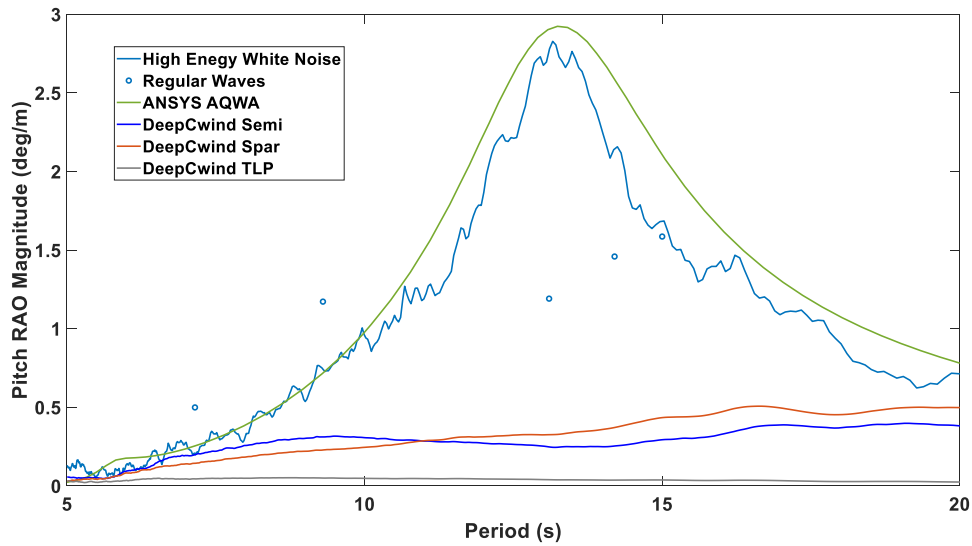


Figure 2.13. High-energy pitch position RAO magnitude comparison

2.5.2. Nacelle Acceleration RAO Magnitudes

The following section presents the results of the nacelle accelerations of the annular model as obtained from experiment, as well as comparisons to AQWA predictions and experimental results for the DeepCwind semisubmersible, spar and TLP. To provide a fair comparison, the accelerations for the all but the TLP are reported at the same point of 81.7 m above the MWL (full scale) for the previously mentioned systems. For the DeepCwind TLP the accelerations were taken at mid-tower, 49.5 m above the MWL due to available data. Nacelle accelerations are particularly important in determining what crucial nacelle parts such as the bearings and gearbox will encounter for inertial loads as the wind turbine is exposed to the offshore environment.

2.5.2.1. Low-Energy Nacelle Acceleration RAO Magnitudes

For the surge nacelle acceleration results of Figure 2.14, all but two of the annular hull irregular wave cases coincide closely with the results obtained from irregular wave testing. As the surge nacelle acceleration is largely influenced by pitch motion, it is no

surprise that a similar trend is found for the pitch position RAO magnitudes provided in Figure 2.10 and Figure 2.13. For the heave acceleration RAO magnitudes of Figure 2.15, the comparison between the white noise and regular wave results is fair.

Comparing the AQWA simulation and experimental results in Figure 2.14, it is apparent that AQWA performs well giving similar surge acceleration RAO trends as well as peak response magnitude and period relative to the test data. Moving to Figure 2.15, the low-energy sea state heave nacelle acceleration RAO results from the model tests and AQWA show significant similarities, but the two peak values apparent in the white noise test data appear at lower periods than those from AQWA.

Results for DeepCwind low-energy nacelle acceleration RAO magnitudes shown in Figure 2.14 and Figure 2.15 are once again significantly lower than those of the annular model. This is most prominent for the nacelle surge acceleration as the experimental results for the annular hull possess an RAO magnitude that is in some cases nearly 90 times greater than the DeepCwind semisubmersible for the wave periods of interest in Figure 2.14. Comparing all the DeepCwind models to the low-energy white noise results for the annular hull, all three models have lower surge acceleration RAO magnitudes for periods ranging from roughly 7 to 15 s. Additionally, the heave acceleration RAO magnitude of the spar is consistently significantly below the annular hull with the exception of the roughly 5 and 9 s periods while the TLP heave acceleration RAO magnitudes are hardly visible due to their extremely small relative magnitude.

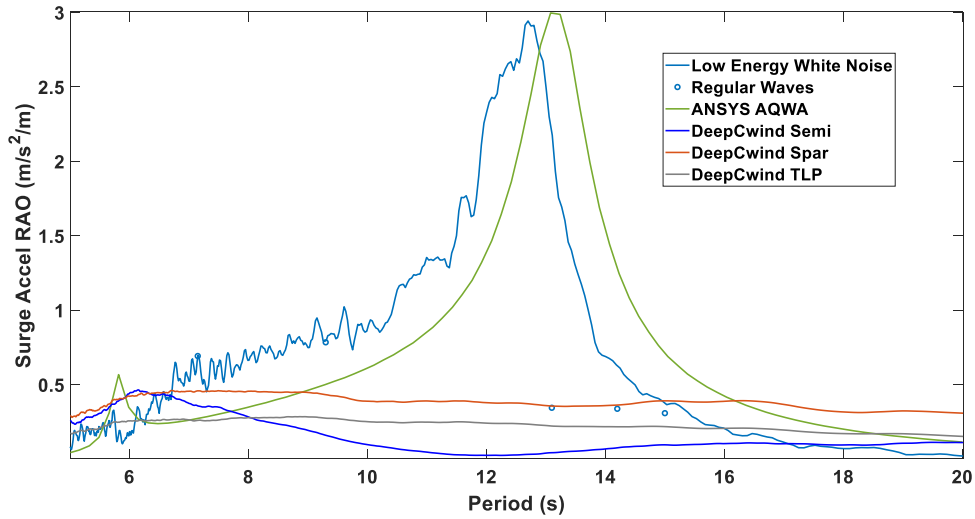


Figure 2.14. Low-energy nacelle surge acceleration RAO magnitude comparison

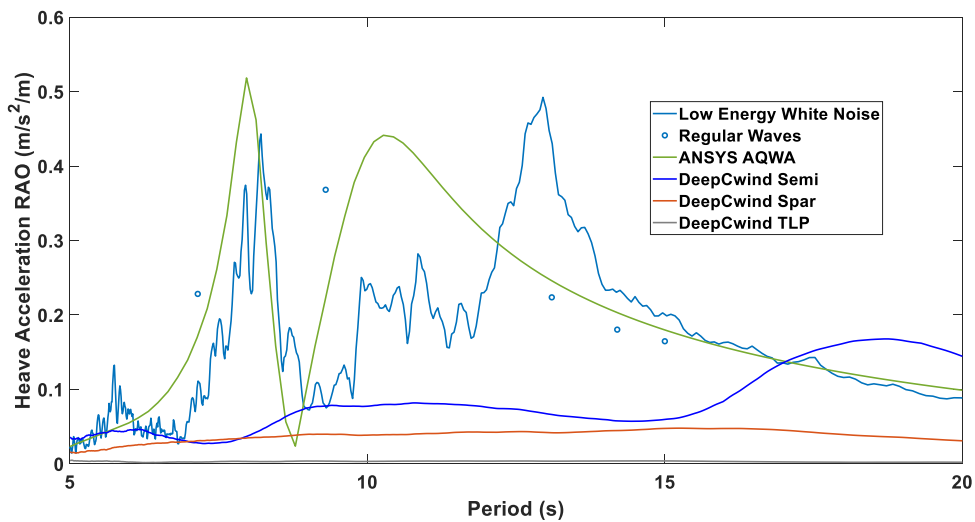


Figure 2.15. Low-energy nacelle heave acceleration RAO magnitude comparison

2.5.2.2. High-Energy Nacelle Acceleration RAO Magnitudes

Referring to Figure 2.16 and Figure 2.17, it is observed that the acceleration RAO magnitudes obtained from the white noise and regular wave tests do not compare as well as those shown in Figure 2.14 and Figure 2.15. The largest discrepancies occur at low wave periods. For the low wave periods, the regular wave amplitudes and motions were

quite small leading to small hydrodynamic damping in the system. For the large white noise irregular wave test, the motions were larger leading to larger hydrodynamic damping, and hence, motion that is likely more strongly damped at these low wave periods. This difference, coupled with the fact that the acceleration RAO is inversely proportional to the wave period squared, yields the greater acceleration RAO magnitude differences observed in Figure 2.16 and Figure 2.17 for small wave periods.

Comparing the AQWA simulations and experimental results of Figure 2.16, it is seen that the peak RAO magnitude for surge acceleration obtained from the high-energy irregular wave data and AQWA analysis are similar over the period range of interest although the magnitude of the AQWA results is noticeably larger from just before the peak period up through the remaining periods. For the heave nacelle acceleration given in Figure 2.17, the RAO magnitudes are over-predicted by AQWA in the range of roughly 11 to 14 s. The AQWA results for heave nacelle acceleration do more closely align with the results obtained for from regular wave testing in this range, however.

With regard to nacelle acceleration of the annular hull system investigated here, it is clear from the RAO magnitudes provided in Figure 2.16 and Figure 2.17 that the DeepCwind semisubmersible system has a significantly lower response over a majority of the period range of interest, particularly for wave periods of 10 s or longer. As was the case for the low-energy sea state comparison, this is most pronounced for the nacelle surge acceleration which exhibits peak RAO magnitudes that are several times larger than the peak heave RAO magnitudes. As shown in Figure 2.16, the annular hull has a lower surge acceleration RAO magnitude than the DeepCwind spar from 5 to roughly 9 s. The DeepCwind TLP has a lower response than the annular hull in Figure 2.16 between 7 and

18 s. The TLP and spar have a relatively consistent RAO magnitude in heave acceleration RAO magnitudes across all studied periods, the magnitude of which is lower than the annular model throughout much of the period range of interest.

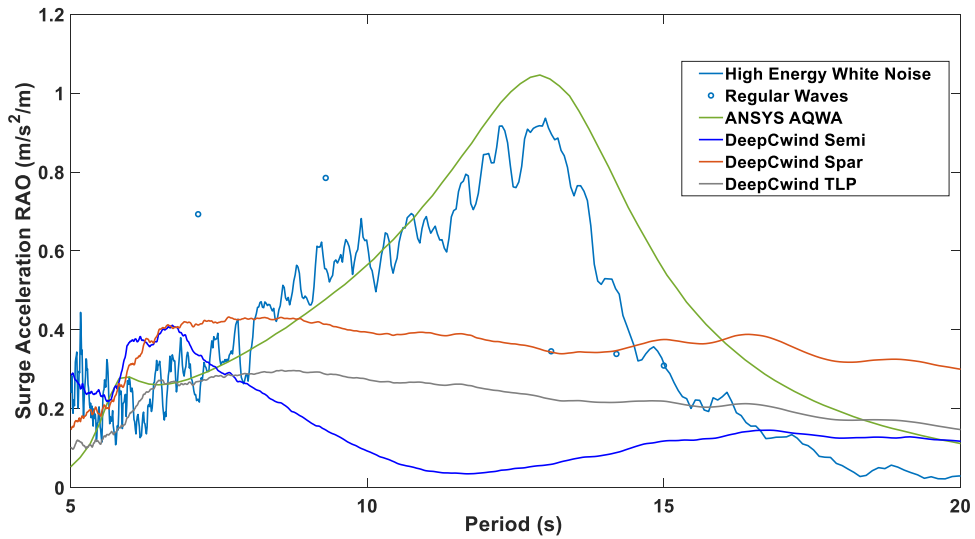


Figure 2.16. High-energy nacelle surge acceleration RAO magnitude comparison

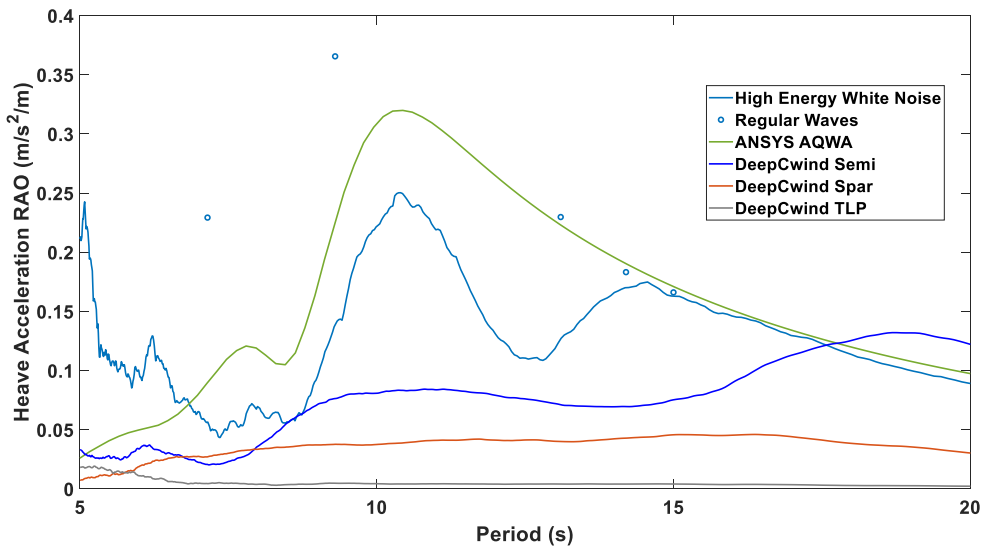


Figure 2.17. High-energy nacelle heave acceleration RAO magnitude comparison

2.5.3. Impacts of Heave Plate Addition

The generic design considered here did not consider any heave plates. A simulation study was conducted with heave plates on the outer perimeter of the hull with

a width of 3.44 m for both the high and low energy wave cases. The only changes to the system were the geometry to account for the heave plates and the calculated viscous damping. Calculation of viscous damping of the system was kept consistent between the baseline models and the models with heave plates with pitch and heave damping corresponding to the percentages of critical as specified previously (4% in pitch and 3% in heave for the low energy wave case and 13% in pitch and 10% in heave for the high energy wave case). Maintaining the percentage of critical damping yielded greater actual damping for the model with heave plates added as the critical damping increases in the pitch and heave DOF due to the increase in added mass provided by the heave plate. Lid damping factors of 0.0001 for the low energy wave case and 0.05 for the high energy case were utilized to maintain consistency with the values utilized in the baseline case. The simulation mesh included 2868 total elements as compared to 1980 total elements in the baseline case.

Comparing the baseline case against the case with heave plates suggests that the heave plates do not significantly impact the RAO magnitudes of interest (Figure 2.18, Figure 2.19). Peak RAO magnitudes in heave for high and low energy wave cases are somewhat higher in magnitude with the addition of heave plates, likely due to the additional wave loading resulting from the plates and their positioning relative to the water surface. In addition, the low energy wave peak resonance in heave occurs at a larger period with the addition of the heave plates with little observable difference in the high-energy case. Peak responses in pitch for both the high and low energy wave cases are similar with and without heave plates with smaller peak responses at slightly larger

periods for the heave plate model. The increase in resonance periods is expected as the heave plates increase system added mass.

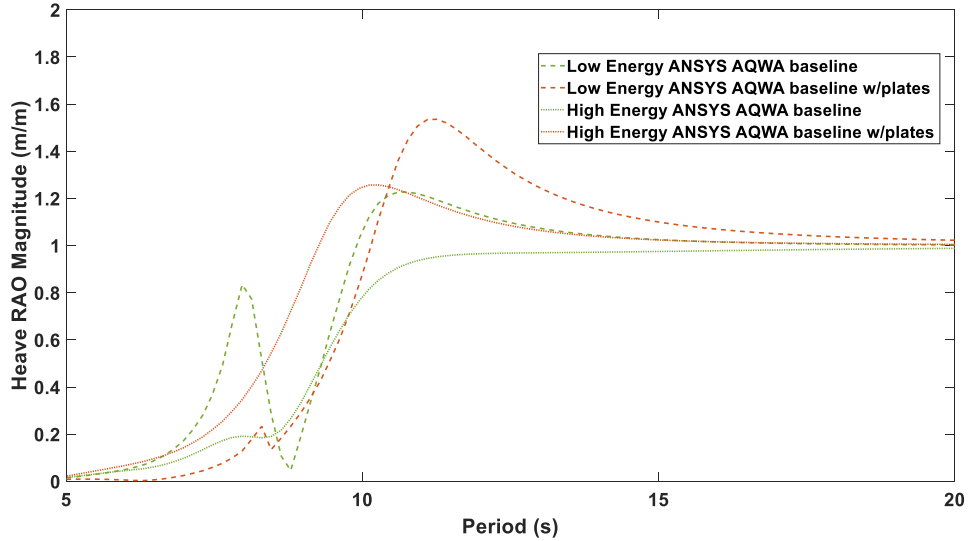


Figure 2.18. ANSYS AQWA heave plate study: Heave RAO magnitude

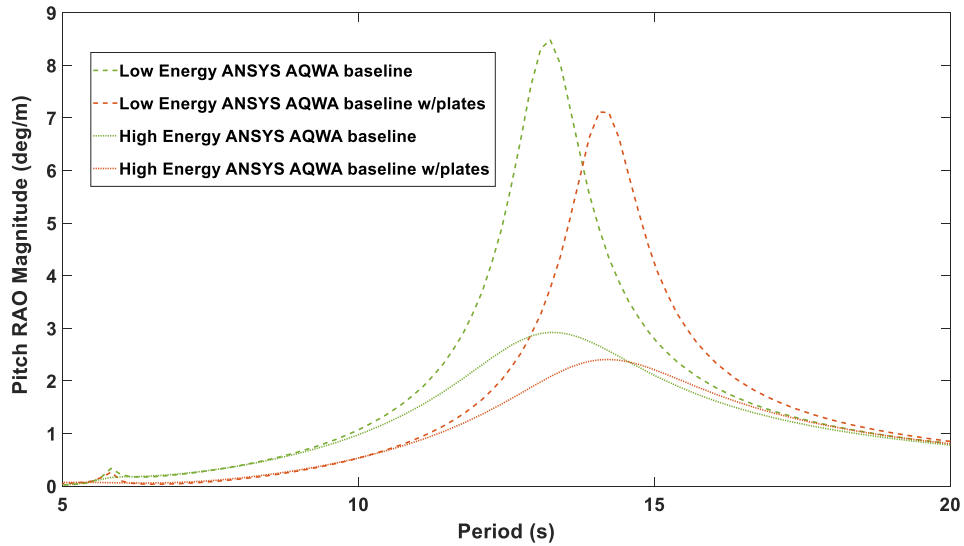


Figure 2.19. ANSYS AQWA heave plate study: Pitch RAO magnitude

2.6. Discussion

Results from experimental and numerical testing of an annular hull were presented in this chapter along with results from the 2011 testing of the DeepCwind

semisubmersible, spar and TLP. The annular system was sized for a 6-MW equivalent turbine while the semisubmersible, spar and TLP from the DeepCwind study were sized for a 5-MW turbine. All results were normalized to account for the discrepancy in turbine sizing. Performance in the categories of position RAO magnitudes as well as nacelle acceleration RAO magnitudes were presented for low and high-energy sea states. It should be noted that the conclusions provided are for the designs as detailed earlier in this work, and may not be applicable to similar designs. It is important to stress that the annular hull model tested here is not optimized and it is quite probable that alteration of system parameters would improve performance. That noted, the DeepCwind FOWT systems are also generic systems and other, more commercially mature versions of these designs may exhibit even better global motion performance than the semisubmersible, spar and TLP comparison data provided here.

2.6.1. Comparison of Response in Low-Energy and High-Energy Sea States

RAO magnitudes derived from low-energy and high-energy white noise wave testing show several differences worthy of noting. Most of these differences, such as reduced peak RAO magnitudes in heave or pitch motion near resonance, are due to the increased platform viscous drag observed in the high-energy sea state testing. These same trends are also observed for the nacelle heave and surge acceleration RAO magnitudes. The surge position RAO magnitude does not vary significantly between the two white noise tests, however, as the surge natural period is far outside the wave periods investigated.

2.6.2. Discrepancy between RAO Magnitudes Derived from Irregular Waves and Regular Waves

For the pitch position and surge acceleration RAO magnitudes, some significant deviation occurs between the regular wave results and the white noise wave results at 13.1 s and 14.2 s wave periods. As these particular periods are close to the natural period of the system in pitch, significant pitch motion occurs which allowed for modest to large amounts of green water and overtopping for these two regular wave test cases (e.g. see Figure 2.7). This significant nonlinear behavior did not manifest itself in the irregular wave cases leading to the significant difference in the two sets of results.

2.6.3. ANSYS AQWA Modeling Capability

This study shows that the use of ANSYS AQWA can provide fairly accurate results for the hydrodynamic response of an annular floating hull. That noted, the accuracy of the results obtained from ANSYS AQWA are dependent on proper tuning of the lid damping factors and external added damping. The values utilized here, while perhaps applicable to a range of potential annular hull designs, are specific to the geometry and wave environments considered in this work.

2.6.4. Performance Comparison for Annular Hull and DeepCwind Platforms

In general, the RAO magnitudes associated with the annular hull are larger than those of the DeepCwind data set. There are a few cases where the annular hull does perform similarly to the other studied systems, namely in surge RAO magnitudes in the range of roughly 15 s to 20 s. The pitch RAO magnitudes in the high and low portions of the period range considered are also fairly similar across all 4 models.

2.6.5. Influence of Heave Plates on Performance

The addition of heave plates resulted in minimal impacts to the system performance. Although the peak response period in heave for the low energy case was extended, the magnitude of system response increased. On a positive note, the period of peak pitch response was extended for both the low and high energy wave cases. Additionally, the magnitude of the pitch response decreased in both cases. The heave plates modeled herein suggest that further optimization would be necessary for improved performance.

CHAPTER 3

COMPARATIVE STUDY OF ANNULAR FOWT HULL GEOMETRIES

3.1. Development of Hull Alternatives

With the performance of a baseline hull quantified, the next step was to explore the impacts of adjusting the geometry. The first portion of geometric adjustments, explored in the following chapter, involves three alternative annular hulls as well as comparison to a basic barge.

3.1.1. Shape Variations

A comparison study of four generic hull geometries was completed to determine the linear hydrostatic stability and rigid-body natural frequencies in the platforms' heave and pitch DOF of each system. Added mass values in surge, heave and pitch are also discussed. Three of the geometries were variations of the annular hull concept: a square prism with a square moonpool, a cylinder with a circular moonpool and a triangular prism with a triangular moonpool. A barge was also studied for a baseline perspective on the effectiveness of adding a moonpool. These options were selected for their relative simplicity, but also for their stark differences in geometry which strongly influences the hydrodynamic loading and moonpool dynamics.

3.1.2. Stability Requirements and Standardized Parameters

All geometries were sized to support a 6-MW turbine with the baseline case taken from Section 2.1. When designing FOWTs, one of the main design constraints is the system's response in rotation about the horizontal axis due to wind and wave loads. As a result, significant focus falls on the pitch RAO. One major factor in determining the pitch RAO is the pitch waterplane stiffness ($K_{pitch\ hydro}$); this characteristic is not frequency

dependent and can be calculated knowing the dimensions of the hull and (3.1) (Jonkman, 2007).

$$K_{pitch\ hydro} = \rho g \iint x^2 dA + \rho g V z_b - m_{tot} g z_g + K_{pitch\ mooring} \quad (3.1)$$

Where: ρ is the density of sea water

g is the gravitational constant

$\iint x^2 dA$ is the area moment of inertia of the waterplane

V is the submerged volume

z_b is the vertical distance to the center of buoyancy

m_{tot} is the total mass

z_g is the vertical distance to the center of gravity

$K_{pitch\ mooring}$ is the pitch mooring stiffness (which is negligible for this analysis)

The pitch waterplane stiffness was calculated for the baseline case and was held constant along with hull height, draft, cross-section width and hull density as well as the other values specified in Table 3.1 and illustrated in Figure 3.1 for all of the designs considered in this section.

Table 3.1. Shape variation standardized parameters

Parameter	Magnitude
Hub Height	100 m
Rotor Diameter	150 m
Turbine Mass	440 t
Tower Mass	520 t
Draft	11.6 m
Pitch Waterplane Stiffness	4,631,000 kN·m/rad
$m_{hull}/m_{ballast}$	7.2
Hull Density	768.0 kg/m ³

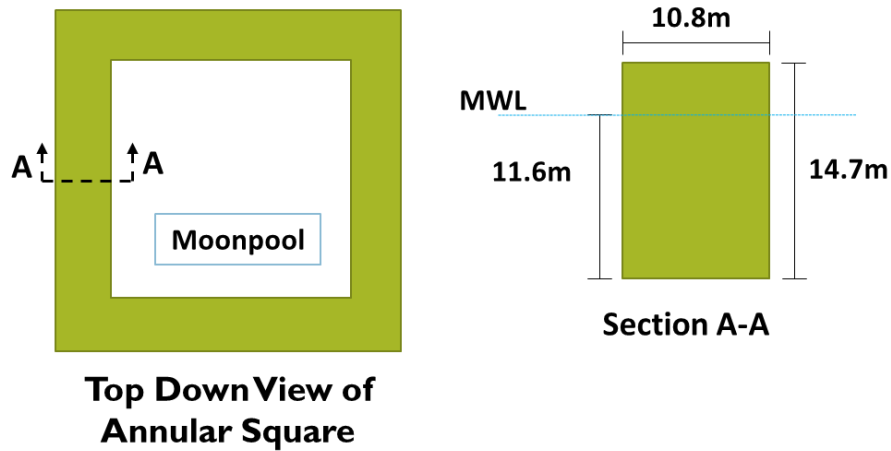


Figure 3.1. Standardized parameter visual

3.2. Shape Comparison Resulting Geometries

Resulting dimensions for the triangular, circular, and barge hulls were determined using the Solver add-on in Excel. The Solver objective value was set as the pitch waterplane stiffness of 4,630,000 kN·m/rad. The dimensional variable for the barge and triangular hulls were the corresponding outer side lengths. For the circular hull the dimensional variable was the outer radius. The variable dimensions were adjusted while maintaining the standardized values from Table 3.1 in order to obtain a design with the desired pitch stiffness. The resulting characteristics are shown in Table 3.2 and Figure 3.2. Figure 3.2 shows the footprints of the hulls with the original square (with moonpool) shown in blue, the triangle in orange, the circle in green, and the outer perimeter of the barge (no moonpool) shown in black. As shown in Table 3.2, the circular hull provides the lowest total mass, the shortest outer perimeter, and the maximum moonpool area. By contrast, the triangular hull represents the highest total mass (of the hulls with moonpool), longest outer perimeter, and smallest moonpool area.

Table 3.2. Selected resulting parameters

Geometry	Total Mass (t)	Floater Mass (t)	Hull Mass (t)	Ballast Mass (t)	Outer Perimeter (m)	Moonpool Area (m ²)
Square	21,341	20,386	17,888	2,498	210	956
Square (no moonpool)	30,638	29,683	26,046	3,637	205	--
Triangle	21,911	20,956	18,388	2,568	228	641
Circle	20,154	19,199	16,847	2,353	191	1,209

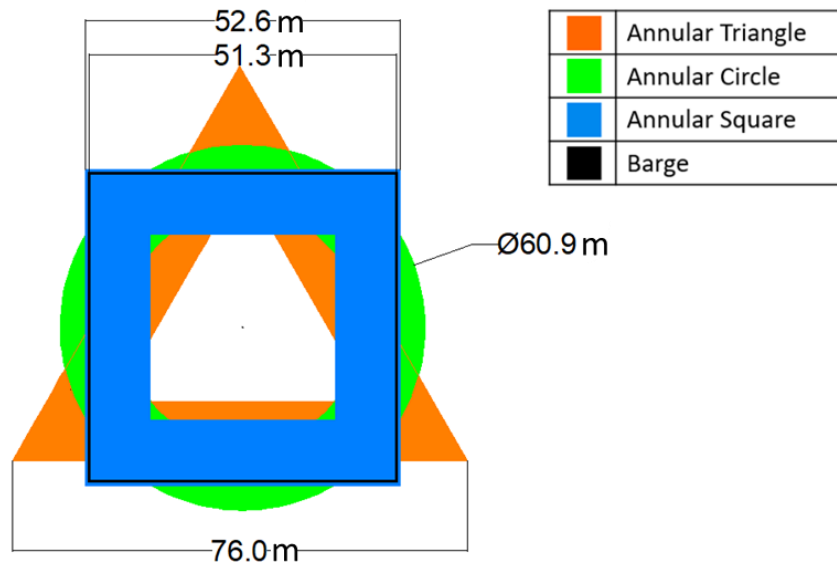


Figure 3.2. Resulting footprints

Additional calculations were completed to determine the inertial inputs for AQWA analysis. Among these are the total system mass, the mass moment of inertia in pitch and yaw about the FOWT's center of gravity and the location of the center of gravity. Inertia values were calculated through the application of the parallel-axis theorem and the assumed mass properties of the hull cross section in Figure 3.1. In general, it was assumed that the hull had uniform density with the exception that the mass of the turbine and tower was also applied in the hull body at a location which mirrored

the surge and sway coordinates of the physical location of the turbine and tower on the horizontal plane. The resulting pitch and yaw mass moments of inertia are given by Table 3.3. For all hulls the center of gravity in the horizontal plane was assumed to be at the intersection of the surge and sway axes. The center of gravity in the vertical (heave) direction was dependent on the mass of the hull and varied from hull to hull as a result; these values are given in Table 3.3 with $z = 0$ falling at the mean water line (MWL) for each hull.

Table 3.3. Shape variation inertias and center of gravity locations

Geometry	Pitch Inertia (kgm ²)	Yaw Inertia (kgm ²)	Vertical Center of Gravity location (m)
Square	1.149×10^{10}	1.859×10^7	-1.053
Square (no moon pool)	1.184×10^{10}	1.380×10^{10}	-2.024
Triangle	8.330×10^9	8.848×10^9	-1.136
Circle	1.181×10^{10}	1.268×10^{10}	-0.865

3.3. ANSYS AQWA Parameters

The following section will discuss the settings applied during modeling in AQWA. Justifications for each setting are also provided.

3.3.1. Mesh Sizing

Per the convergence study completed in the numerical modeling section (Section 2.4), a sufficiently refined mesh was applied to each of the models studied herein. All four of the models were meshed with a defeaturing tolerance of 1 m and a maximum element size of 4 m. Table 3.4 specifies the total number of nodes and elements for all four hull forms.

Table 3.4. Mesh characteristics

Geometry	Number of Nodes	Number of Elements
Square	2025	1980
Square (no moon pool)	969	924
Triangle	1265	1216
Circle	1847	1806

3.3.2. Modeling Parameters

The global response of the four systems of interest were simulated in ANSYS AQWA with the moonpools modeled using the external lid feature. Each geometry was subjected to a range of wave periods from 5 s to 20 s in increments of 0.23 s. The waves were applied along the surge direction at 0 degrees (see Figure 3.3). For the triangular hull the waves approached from the broad side. In addition to the runs completed in AQWA, the same parameters were applied to the square annular hull model and run in the commercial modeling software WAMIT as verification for the ANSYS AQWA results for the heave and surge RAO results.

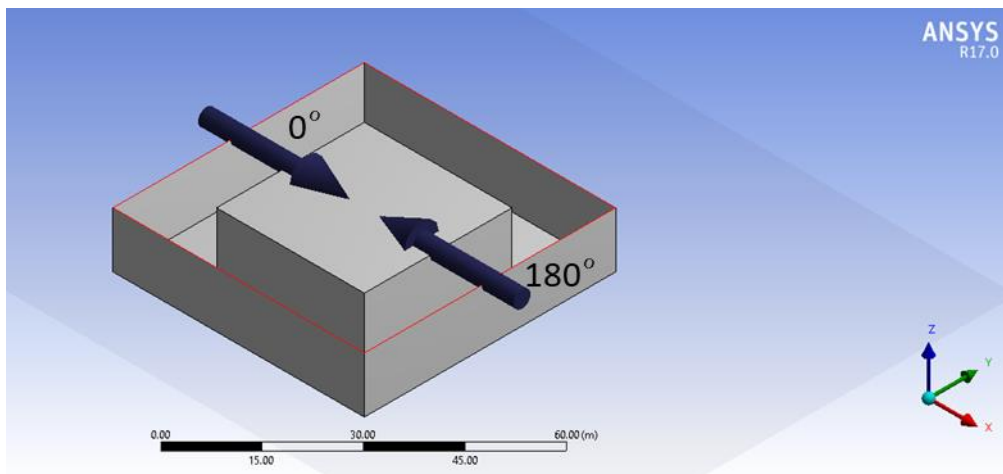


Figure 3.3. Square annular hull with wave directions

3.3.3. Assumptions and Simplifications

Each hull supported a 6-MW turbine with a mass of 438 metric tons. The turbine tower mass was also standardized at 517 metric tons. In the sizing process the hull height, draft, cross-section width and hull density were kept consistent across all four designs. The effects of mooring lines were not included in this study as they have a negligible impact on system motions in the wave frequency region.

The additional external damping due to viscous effects was tuned for the high energy set of wave cases as prescribed by section 2.4. As such, the external damping inputs were approximated similarly across all models. The damping for each model was determined using a damping ratio of 10% of the critical damping in heave and 13% of the critical damping in pitch with critical damping calculated as specified in (3.2) (Inman, 2001).

$$\zeta = \frac{c}{c_{cr}} = \frac{c}{2\sqrt{K_i m_{tot}}} \quad (3.2)$$

Where: c is applied damping
 c_{cr} is critical damping
 K_i is the stiffness in pitch or heave
 m_{tot} is the mass (or inertia in the case of pitch)
 ζ is the damping ratio

The heave critical damping is approximately equal to the value utilized for the high energy sea state and the pitch critical damping value is approximately equal to that utilized for the low energy sea state in section 2.4. Additionally, all three annular hulls utilized a value of 0.05 for the lid damping factor matching the value specified for high energy sea states in section 2.4 (see Chapter 2 for impacts of varying this value). Per the ANSYS User's Manual the width of the lid was specified as the width across the

moonpool (ANSYS Inc., 2013b). In the case of the triangular and circular hulls the widths were taken as the mean width across the corresponding moonpool.

As noted previously, the study completed only considered unidirectional waves. The wave cases considered here run along the x axis. The wave in the zero-degree direction was used to generate all RAO magnitude plots which represent a wave running from the positive x-direction to the negative x-direction. In the case of the offshore environment it would be important to consider waves from multiple directions, particularly in the case of the square and triangular systems as the geometry is not symmetric and would likely change the system response more than the symmetrical circular system.

3.4. Results

With the system geometries determined, additional system characteristics were calculated and compared with AQWA results. The natural periods, added masses, and RAO magnitudes for each geometry are specified below.

3.4.1. Natural Periods

Following the determination of the dimensions, the pitch and heave natural periods were calculated manually as part of the comparison and verification process. The pitch natural periods ($T_{n_{pitch}}$) were calculated according to (3.3) (Halkyard, 2013). The heave natural periods ($T_{n_{heave}}$) were calculated according to (3.4) (Halkyard, 2013). The results of these calculations are shown in Table 3.5.

$$T_{n_{pitch}} = 2\pi \sqrt{\frac{K_{pitch\ hydro} + K_{pitch\ mooring}}{I_{pitch} + I_{pitch\ added}}} \quad (3.3)$$

Where: $K_{pitch\ hydro}$ is the pitch stiffness
 $K_{pitch\ mooring}$ is the mooring stiffness in pitch (considered negligible)
 I_{pitch} is the pitch inertia of the system
 $I_{pitch\ added}$ is the pitch inertia of the added mass per AQWA

$$T_{n_{heave}} = 2\pi \sqrt{\frac{K_{heave\ hydro} + K_{heave\ mooring}}{m_{tot} + m_{heave\ added}}} \quad (3.4)$$

Where: $K_{heave\ hydro}$ is the pitch stiffness
 $K_{heave\ mooring}$ is the mooring stiffness in heave (considered negligible)
 m_{tot} is the mass of the system
 $m_{heave\ added}$ is the added mass in heave per AQWA

Table 3.5. Pitch and heave calculated natural periods

Geometry	Pitch Natural Period (s)	Heave Natural Period (s)
Square	11.6	10.1
Square (no moon pool)	11.9	11.2
Triangle	10.4	10.2
Circle	11.7	9.3

These calculated values serve as approximate values for the location of peak values on the pitch and heave RAO plots which indicate resonance. Because each of these periods is calculated considering a fixed approximation of the added mass—which is actually frequency dependent—the exact period with maximum response can be somewhat different than the natural period.

3.4.2. ANSYS AQWA Added Mass

Components of added mass reflect the mass of the volume of water that moves when the structure moves. Added mass is one factor in determining how a system will respond in a wave environment. The plot of the surge added masses (Figure 3.4) shows that the circular hull has the highest peak value for surge added mass. However, all three

designs with moonpools have approximately the same added mass at the 20 s wave period ($\sim 2.5 \times 10^7$ kg). As the surge natural period of these systems when moored tends to be quite long, the results of Figure 3.4 indicate that the contribution of the surge added mass of all three systems to the natural period is effectively the same, which given their similar physical masses, indicates that all three systems will likely exhibit near equal surge natural periods. Comparing the barge and annular hull systems, the faces of the moonpools for the models that have them contribute additional added mass, hence the increase in surge added mass relative to the barge system.

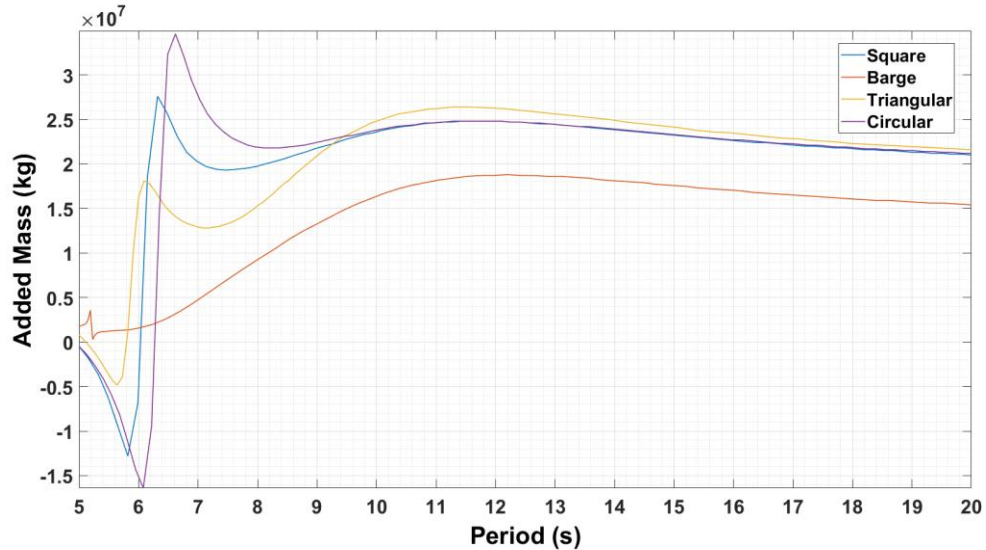


Figure 3.4. Shape variation surge added mass

The plot of the heave added masses (Figure 3.5) shows that of the four geometries simulated, the barge has a significantly higher value for heave added mass at all evaluated periods. The triangular hull has the second highest and square hull and circular hulls are the third and fourth largest, respectively. For this DOF it seems reasonable for the barge to have the highest value of added mass as it has the largest waterplane area.

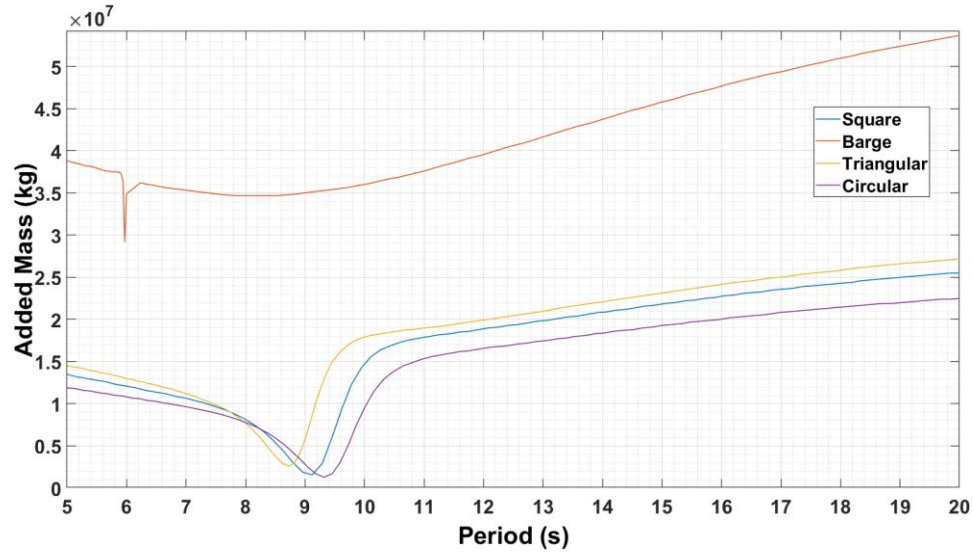


Figure 3.5. Shape variation heave added mass

A plot of the pitch added inertias for the systems studied (Figure 3.6) shows that the circular hull has the highest peak magnitude. Again, all three designs with moonpools have approximately the same added inertias as the wave periods increase. In this case the barge has the highest added inertia. The added inertias in the pitch DOF are dependent in part on the waterplane area of the hull (hence the gap from the moonpool hulls to the barge), but also on the way this area is distributed. As the barge water plane area is not only solid, but also has a perimeter almost similar in size to the other designs, it is not surprising that the pitch added mass is in general larger than the annular hull systems for most wave periods studied.

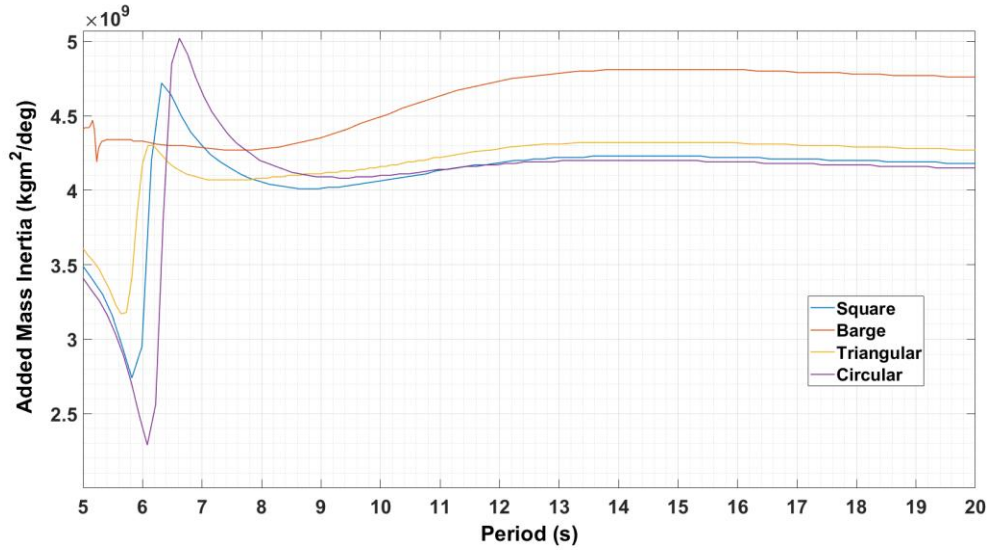


Figure 3.6. Shape variation pitch added inertias

3.4.3. ANSYS AQWA Response Amplitude Operators

The physical response of the structure due to interactions with the waves is a critical design consideration. As a result, RAO magnitudes for three DOFs (surge, heave, and pitch) hold a substantial amount of weight in the comparison process. As shown in Figure 3.7, the barge has the highest peak surge RAO magnitude.

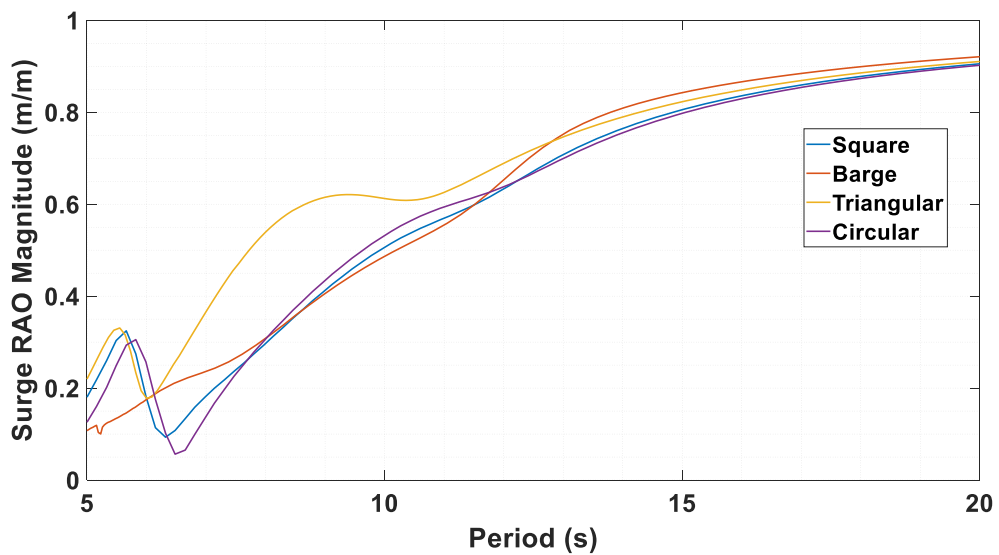


Figure 3.7. Shape variation surge RAOs

All four models exhibit a similar trend of increasing RAOs with increasing periods with two separate downward trends. One of the downtrends is at roughly the 6 s period. For the square annular design, this downtrend is very close to the sloshing natural frequency of the moonpool of 6.35 s. In the cases of the triangular and circular hulls, the sloshing natural frequency is a bit more difficult to calculate as the equation for calculating the natural frequency uses the width of the moonpool as an input. When referring to the square geometry, it is reasonable to say that the “width” of the moonpool is the side length. For the circular hull, the moonpool does not have any faces which would be categorized as sides in the same way, but approximating the width to be the average width of the circle results in an approximate natural period for the sloshing mode of 6.36 s which is in general agreement with the observations of the ANSYS AQWA simulation results. In the case of the triangle, for the wave at zero degrees, the side length of the moonpool varies from 0 m at the point to 38.47 m at the side of the triangle. Considering the width to be the average width of the moonpool results in a sloshing natural period of 7.98 s; the AQWA results suggest that a value of 6 s is more realistic. The second downtrend is near the 12 second period (10 seconds for the triangular hull). This downtrend is likely due to a canceling effect as the length of the hulls in the surge direction is similar to the wavelength associated with the period.

Each of the moonpool hulls has a notable drop in the heave RAO (Figure 3.8) at a similar period. It is likely that this slight dip is influenced by the natural period of the moonpool piston period. The calculated piston natural period values (per section 1.2.3) for the moonpools of the square, triangular and circular hulls are 9.88 s, 9.40 s, and 10.20 s, respectively. The calculated heave natural periods of the systems are 10.09 s, 10.19 s,

and 9.27 s, respectively, which are very close to the predicted piston periods. By contrast, the periods in the low point of the dips for the three annular hull heave RAOs occur at 8.27 s, 8.36 s, and 8.46 s, these values not aligning with the anticipated heave periods or moonpool piston periods. This discrepancy suggests that this dip is caused by coupling between the resonant vertical motions of the hull and the water in the moonpool. Overall, the circular hull has the highest peak heave RAO magnitude and it is followed by the square, triangular, and barge hulls, respectively. The heave RAOs for all four systems at large periods are almost identical. Although the barge system does not seem to experience the damping that the annular hulls do, it does outperform the other systems across the full range of the periods with the exception of the periods in proximity to the downtrends from the other hulls where the moonpool piston motion damps the hull motion.

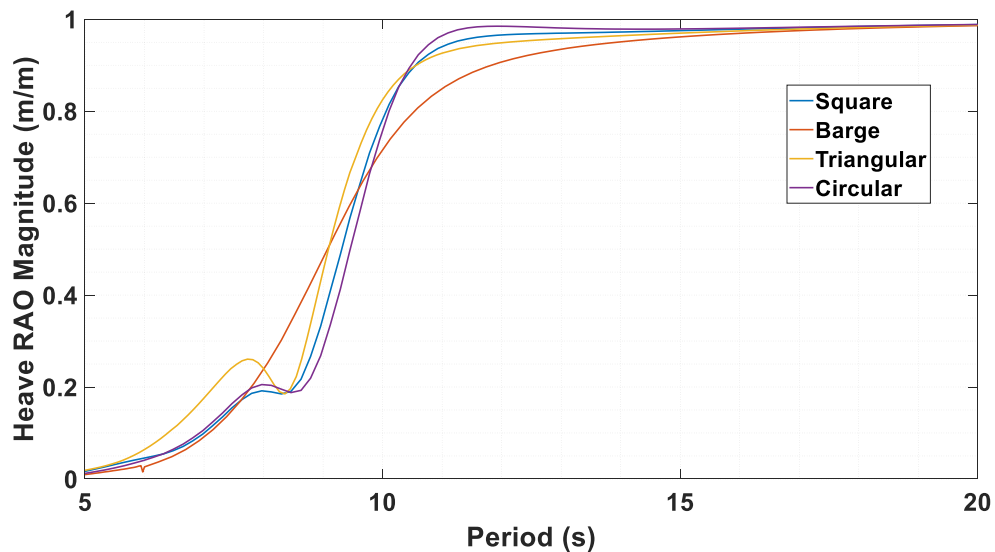


Figure 3.8. Shape variation heave RAOs

The pitch RAO magnitudes shown in Figure 3.9 suggest that the geometry does not have a significant impact when comparing the square, barge, and circular hulls. The peak values for each of these geometries are all very similar. On the other hand, the peak

value and peak period of the triangular hull response are both slightly lower than the rest of the group. The pitch DOF is not considered to be significantly influenced by the moonpool as calculated pitch natural periods align well with peak values from Figure 3.9. Calculated values for the square, triangular and circular hulls are 11.56 s, 10.36 s, and 11.66 s respectively while the peak values from AQWA are 11.76 s, 10.60 s, and 11.92 s.

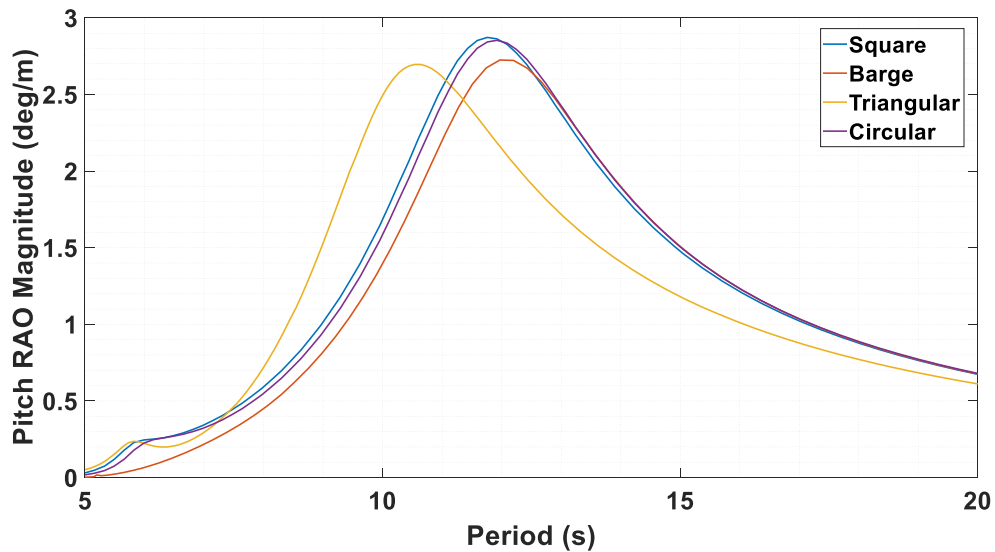


Figure 3.9. Shape variation pitch RAOs

3.5. Discussion

The results of this study suggest that there is not a significant difference in the global performance as determined by RAO magnitudes for the four modeled systems in surge, heave, or pitch DOF. It does show, however that using the outer dimensions of a barge system and transitioning it into an appropriately-sized annular hull can significantly reduce the volume of material needed to support a turbine of equal size. In comparing the three annular hulls the square and circular hulls performed very similarly across all three RAOs. The triangular hull had a larger surge response than the square and circular hulls from roughly 7 s to 10 s. Although the peak response in pitch for the triangular hull is

smaller in magnitude than the circular and square hulls this is not enough to make up for the impracticality in fabricating a hull with a larger footprint. The final comparison between the circular and square hulls considers the ease of fabrication and storage along with transportability. From a manufacturing standpoint the square hull is considered to be better as it can be manufactured in segments using primarily right angles and forms that feature the same. By comparison, fabrication of the circular model would require arched forms to produce the circular shape which are not readily available. In addition to this, the maneuverability of a square is easier when considering moving the hull around dry docks and other port facilities due to the general shape of the environment as well as its side length which offers a smaller minimum dimension. Based on consideration of these additional areas of interest, the square hull is the superior option and is chosen as the ideal hull of those tested.

CHAPTER 4

SIZING OPTIMIZATION OF SQUARE ANNULAR HULL

4.1. Introduction

The intent of the following optimization was to design an efficient, high-performance annular FOWT hull through the minimization of the pitch natural frequency and system mass using a Genetic Algorithm (GA) documented in Goupee and Vel (Goupee & Vel, 2007). The GA from Goupee and Vel uses a particular real-coded elitist non-dominated sorting multi-objective GA known as NSGA-II (Non-dominated Sorting Genetic Algorithm-II) from the work of Deb et al. (Deb et al., 2000). NSGA-II was created to combat the typical shortfalls of NSGA including its high computational demand and lack of elitism. Goupee and Vel utilized this GA to optimize the functional grading of materials to best utilize the inherently inhomogeneous material properties.

4.2. Optimization Problem Statement

The general form of a constrained optimization problem includes design variables to be modified, bounds on those variables, functions to be optimized, and constraints on the results. The complete problem statement for this optimization problem is as follows:

$$\begin{aligned} &\text{Find} && P1, P2, P3, \text{ and } P4 \\ &\text{Minimize} && f1 = \frac{m_{tot}}{m_{nom}} \ \& \ f2 = \sqrt{\frac{K_{pitch \ hydro}}{I_{pitch} + I_{pitch \ added}}} \\ &\text{Subject to} && \omega_{pitch \ nom} \\ &&& g_1 = \frac{7m - t}{t_{nom}} \leq 0 \\ &&& g_2 = \frac{height - draft}{draft_{nom}} \leq 0 \\ &&& g_3 = \frac{-K_{pitch \ hydro}}{K_{pitch \ nom}} \leq 0 \end{aligned}$$

$$g4 = \frac{\theta_{pitch} - 10^\circ}{10^\circ} \leq 0$$

$$g5 = \frac{2m - freeboard}{2m} \leq 0$$

$$10m < P1 < 60m$$

$$30m < P2 < 74m$$

$$0m < P3 < 15m$$

$$5m < P4 < 30m$$

Where: $P1, P2, P3$ & $P4$ are hull geometric parameters (see Figure 4.1)

m_{tot} is system mass, kg

m_{nom} is mass of baseline system without heave plates, kg

$K_{pitch\ hydro}$ is pitch stiffness, N·m/rad

I_{pitch} is pitch inertia, kg·m²

$I_{pitch\ added}$ is pitch inertia from the added mass, kg·m²

$\omega_{pitch\ nom}$ is nominal pitch natural frequency, rad/s

t is hull thickness, (P2-P1)/2, m

t_{nom} is nominal hull thickness, m

$height$ is hull height, m,

$K_{pitch\ nom}$ is nominal pitch stiffness, N·m/rad

θ_{pitch} is platform pitch angle under wind turbine thrust at rated wind speed, degrees

$freeboard$ is distance from waterline to top of hull, m

4.2.1. Objective Functions

The objective functions are $f1$ and $f2$. The mass ratio ($f1$) is calculated by taking the mass of the proposed geometry and comparing it to the nominal mass of 2.134×10^7 kg as described in the model specifications in Table 2.1. The benefits of mass reduction include a smaller footprint and material reduction, both of which are important to reducing cost and easing the burdens of transportation and installation. The pitch natural frequency ratio ($f2$) is calculated by taking the pitch natural frequency of the system (the square root of the pitch stiffness divided by the pitch inertia) and dividing it by the nominal pitch natural frequency of 0.544 rad/s (or 0.087 Hz) per the specified value from Table 2.1. Minimizing the FOWT's rigid-body pitch natural frequency ratio results in

increasing the pitch natural period of the system further. Longer natural pitch periods are helpful in preventing resonance from the excitation of typical offshore sea state conditions. The intent is to minimize both of these functions, but their ideal geometries compete; that is to say that for the pitch natural frequency of f_2 to decrease, the mass ratio of f_1 is typically increased and vice versa. The competition between these two objective functions makes this scenario a prime candidate for the multi-objective optimization provided by NSGA-II.

4.2.2. Design Variables and Corresponding Bounds

For this case, the design variables of the hull which are subjected to optimization techniques are P_1 , P_2 , P_3 , and P_4 , as illustrated in Figure 4.1.

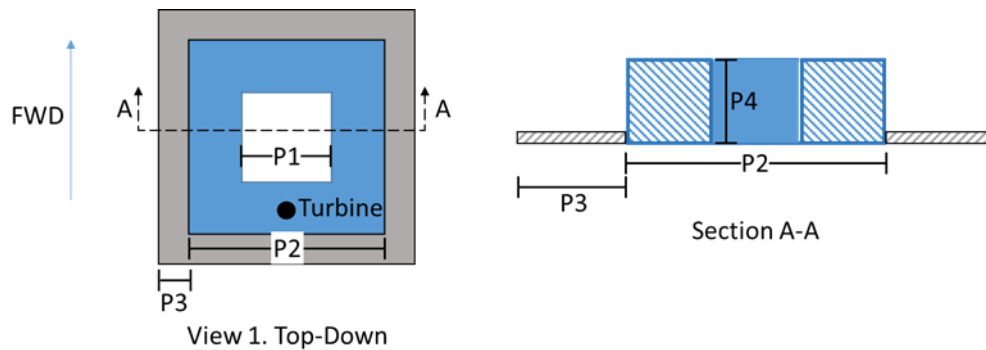


Figure 4.1. Top-down and section view of hull

The thickness of the heave plate (shown in grey in Figure 4.1) is kept consistent across all variations at a value of 0.457 m per industry recommendation. The heave plate is always mounted with its lower edge aligned with the base of the hull. Additional constants are listed in Table 4.1. Hull density is an average value assuming that the ballast is evenly distributed throughout the hull. The design variables will be used to determine the system mass, center of gravity, mass moments of inertia, and natural period in pitch using MATLAB.

Table 4.1. Constant values

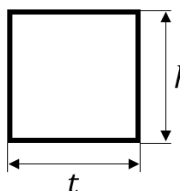
Constant	Value (kg/m ³)
Sea Water Density	1,025
Hull Density	768
Plate Density	1,895

The calculation of system mass is based on the volume of the hull multiplied by the density and adding that to the product of the plate density and volume as well as the turbine and tower masses. The center of gravity of the system uses the masses of each of the components coupled with each of their corresponding center of gravity in the horizontal x and vertical z directions relative to aft left corner on the mean waterline.

The pitch natural period of the system is highly dependent on the pitch stiffness which was previously defined in Chapter 3 and is driven by the waterplane area, submerged volume and vertical position of the center of gravity. The other input for the pitch natural period is the pitch inertia. The pitch inertia of the hull and heave plate are derived from component inertias.

In addition to the system itself, there is also the influence of the added mass on the inertia of the hull. Added mass is an additional resistance to motion of a body in a fluid which is the result of the acceleration of the body. The added masses are approximated for the purposes of this analysis according to guidelines from Appendix D of Det Norske Veritas RP C205 (Det Norske Veritas, 2014) as well as the parallel axis theorem. Utilized added mass coefficients are given in Table 4.2 with the relevant equation for added mass ($m_{heave\ added}$) given in (4.1). All calculations are detailed in the MATLAB scripts in Appendix A.

Table 4.2. Added mass coefficients

Hull Cross Section	$\frac{t}{h}$	Direction of Motion	C_A	A_R
	∞	Vertical	1.0	$\pi \left(\frac{t}{2}\right)^2$
	10		1.14	
	5		1.21	
	2		1.36	
	1		1.51	
	0.5		1.70	
	0.2		1.98	
	0.1		2.23	

Where: h is hull draft or heave plate thickness
 t is hull thickness or heave plate width

$$m_{heave\ added} = \rho C_A A_R \quad (4.1)$$

Where: $m_{heave\ added}$ is heave added mass of from the hull or heave plates

Restrictions on the geometry come from bounds which are specific to the variables themselves. Upper and lower bounds on $P1$, $P2$, $P3$, and $P4$ are given in the problem statement in section 4.2. The intent of the bounds is to keep the footprint and hull height values from becoming unreasonable or unrealistic, mostly from a manufacturing perspective. Additionally, variables are kept in the positive design space to allow for physical existence of the hull. The width of the moonpool ($P1$) can vary from 10 m to 60 m. The lower bound forces the existence of the pool while the high end of the range coupled with the upper bound of the hull width ($P2$) of 74 m helps to ensure both a comparable or more efficient footprint as well as the ability to support the diameter of the base of the wind turbine tower. The lower bound on the hull width (30 m) is slightly smaller than the width of the hull for a 2-MW turbine, allowing hulls with smaller widths,

but other geometric variations to be explored. The heave plate width ($P3$) is permitted to vary from 0 m to 15 m, representing the hull as tested and numerically validated in Chapter 2 as well as the potential for the addition of heave plates. Upper and lower bounds on the height of the hull force the hull to be a maximum of a typical hull height for a 6-MW FOWT hull of 30 m and at a minimum to be able to have a 3 m draft while allowing 2 m of freeboard. In addition to the justifications provided above, the bounds serve to expedite the evaluation as their existence reduces the design space to a more manageable volume for the scope of this task.

4.2.3. Constraints

While the objective functions set the stage for the problem to be solved, the constraint functions form guidelines on the geometry and basic system performance. The first constraint function ($g1$) serves to ensure that the side lengths of the moonpool are smaller than those of the hull, thereby allowing for the physical existence of the system. The second constraint function ($g2$) forces the draft of the system to be less than the height of the hull, which guarantees that the system can float. The purpose of the third term ($g3$) is to drive the pitch stiffness of the design to be greater than zero; a condition which would present no resistance to overturning. Constraint function $g4$ serves to help maintain the static pitch displacement to be no more than 10 degrees under a baseline wind loading case. This constraint is based on maximizing wind turbine functionality, as tilted rotors capture less energy and turbine manufacturers do not design their turbines to function for scenarios where the turbine is tilted far from perfectly vertical. The final constraint ($g5$) pushes designs to feature a freeboard which will experience limited greenwater in day to day operations. Each of the five constraints will yield unique values

for each combination of design variables depending on the degree of violation for any particular value. The resulting values of each of the five constraint functions are summed to form one total constraint value.

4.3. Use of NSGA-II Optimization Technique

Using the NSGA-II optimization technique, the first step in finding an optimal set of solutions is to generate a random population of N individuals; for this optimization N is 100. These individuals represent a chromosome made up of the four design variables (genes). Each individual is evaluated against the two objective functions to determine their fitness. The individuals are also evaluated to obtain a measurement of constraint violation. For this formulation, the constraint violation is applied as a constraint value (cv) which represents the sum of the values of each constraint function as shown in section 4.2.

The goal of this optimization is to generate a set of possible geometries for the objective functions known as Pareto-optimal solutions or a Pareto front. These solutions represent a population which is non-dominated throughout the feasible design space (Pareto, 1971). For some individual A to constrain-dominate some individual B, any one of a set of the following three conditions must be true:

1. Both A and B are feasible, with
 - a. A being no worse than B in all objectives
 - b. A is better than B in at least one objective
2. A is feasible and B is not
3. A and B are both infeasible, but B has a larger constraint violation

If none of the three conditions are true, A and B are non-dominated (Goupee & Vel, 2007).

Even if a solution is considered to be dominated within the current generation, it can still be carried through to the next generation. After each member of the population is evaluated, they are given a rank of non-constrain-domination. Non-dominated individuals are given a rank of 1; individuals which are only dominated by those individuals with a rank of 1 are given a rank of 2, and so on. This rank will be applied later in the process.

An additional factor in the selection of individuals is the crowding distance. Crowding distance is a measure of proximity of an individual to neighbors of equal rank. Evaluating the crowding distance encourages a more diverse population which helps to ensure that a variety of possible solutions are evaluated. The metric used here is taken from Deb et al. (Deb et al., 2000).

Once the population has been established, the next goal is to create an offspring population. For a multi-objective GA, this means the creation of a mating pool. The mating pool represents the population from which the parents of the next generation will be selected. To determine which individuals enter the mating pool, two individuals from the population of size N are selected at random to compete in a tournament. The winner between some individual A and some individual B is the individual with the better rank or the individual with the larger crowding distance in the event that they have the same rank. A copy of the winner is added to the mating pool. This process is complete when each individual has competed twice and the mating pool consists of N parents. As a result of the tournament selection process the mating pool now contains more copies of stronger individuals and fewer copies of weaker individuals.

The creation of the next generation is completed next by randomly choosing two parents from the mating pool and applying simulated binary crossover (SBX) and the real-parameter mutation operator to create two children. The children are evaluated for their resulting objective function values as well as their respective constraint violations. The creation of children is complete when all parents have gone through crossover and mutation. The offspring population contains N children.

Although the children have been created, the finalized population of the next generation is not yet complete. The next step in the process is to combine the population of children with the population of parents. The population is then assigned updated ranks based on the total population and then sorted by increasing rank. A new crowding distance is assigned to each individual within each rank. The individuals within the rank are sorted from largest to smallest crowding distance. With the sorting complete, the new population is taken from the top N solutions within the list. This final step in the process represents utilization of the principal of elitism.

The entire process is repeated for the construction of each new generation. For this analysis, a population of 100 individuals—each of four genes—produces 100 generations in the Pareto-optimal set. Much of this process takes place within the Matlab algorithms from Goupee and Vel, but one major difference occurs in the ‘myfuns.m’ Matlab function. This function is where the optimization process is customized to evaluate the objective functions and constraints pertaining to a particular problem statement. Evaluation of various geometrically dependent parameters such as system mass, hydrostatic stiffness, natural periods and more occur in ‘myfuns.m’ which allows

for the determination of associated objective function values and constraint values as discussed in sections 4.2.1 and 4.2.3.

4.4. Results

For this particular problem, as the algorithm moves from generation to generation the individual designs tend to cluster together before forming the Pareto Front. The scatter shown in Generation 1 in Figure 4.2 demonstrates the randomness in the initial population.

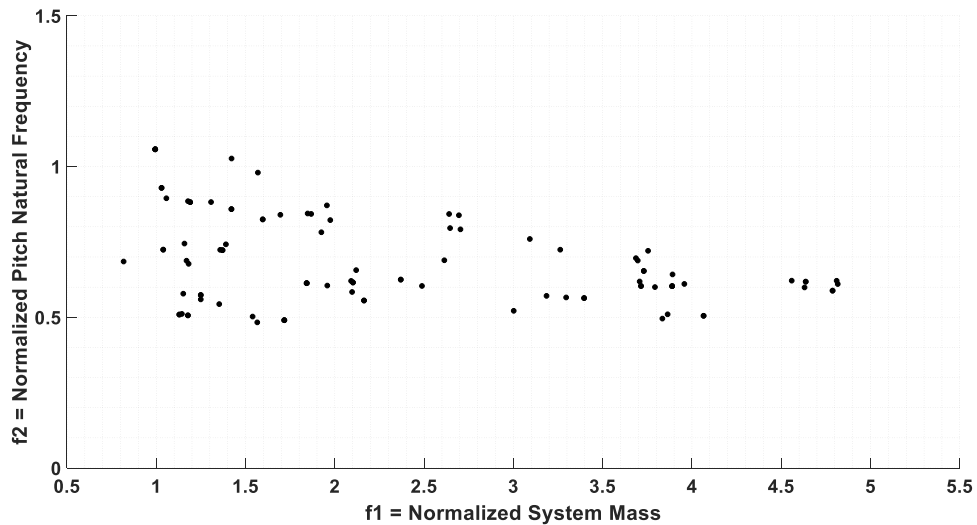


Figure 4.2. NSGA-II Generation 1

As early as the tenth generation (Figure 4.3), the locations for optimal solutions start to emerge as the maximum value of the mass ratio decreases and beginnings of the Pareto front emerge. As the population continues to change from generation to generation, the resulting population begins to form two relatively linear groupings; this is clearly shown in Generation 50 in Figure 4.3.

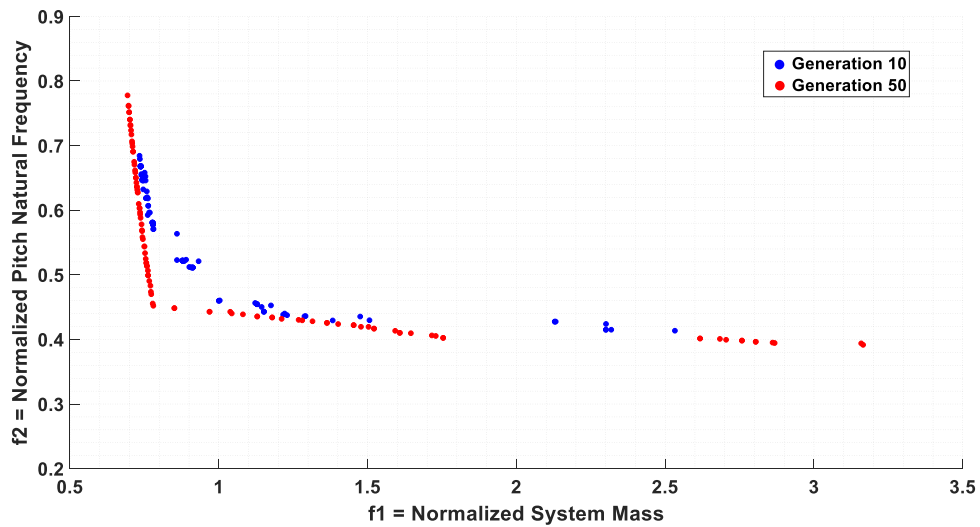


Figure 4.3. NSGA-II Generation 10 and Generation 50

Figure 4.4 shows three solutions selected from Generation 100 which represent the significant variation in geometries of the final result. Geometry A provides the lowest system mass while geometry C provides the lowest pitch natural frequency among the population. Solution B illustrates a geometry which represents a solution which has only slightly more mass than solution A, and only a bit higher platform pitch natural frequency than solution C. The existence of a solution such as design B illustrates the power of performing a multi-objective optimization as it performs well in all objectives while only making small performance concessions to other designs which only perform slightly better in one objective, but much worse in the remaining objective. All geometries are approximately to scale.

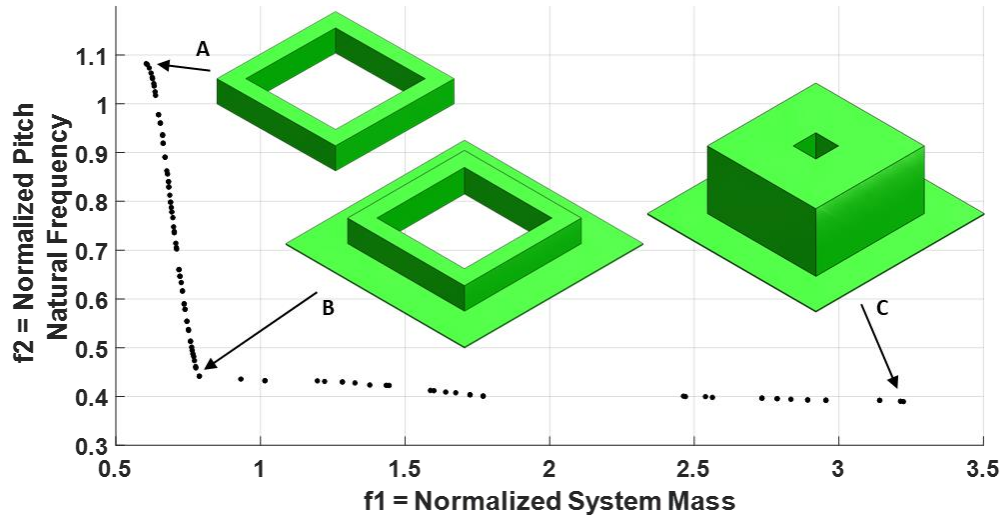


Figure 4.4. NSGA-II Generation 100

Results (see Appendix B) from the NSGA-II run reveal a tendency for the optimal moonpool dimension to be between 11.34 m and 44.0 m, these values being well within the bounds set for this optimization variable. Additionally, the optimal hull width is very close to the upper limit ranging from 54.0 m 58.1 m. The various combinations of these dimensions force the width of the hull segment to stay between 7 m and 21.5 m. The width of the heave plates along the Pareto front occupy the entirety of the allowable range, with values of 0 m to 15 m. The hull height varies within the top two thirds of its bounds, with the lowest value at 10.8 m and the highest value at the upper bound of 30 m. The smallest normalized pitch frequency occurs when the heave plate width is towards its upper bound at a value of approximately 15 m and the height of the hull is also near its upper bound at approximately 30 m. By contrast, the smallest ratio of mass to the nominal value is achieved when the heave plate width is approximately 0 m and the hull height is approximately 10.9 m. This constitutes a design with a height that is roughly one third of the height for the optimal geometry for minimization of pitch natural frequency.

A tabulation of key characteristics of geometries from designs A, B, and C from the Pareto front are given in Table 4.3. These results illustrate the true competing nature of the two objective functions. Geometry A represents the minimum value of the mass ratio objective while geometry C represents the minimum value of the pitch natural frequency. Geometry B is a geometry which approximately represents the best case for compromise between both objective functions. The values for $P1$, $P2$, and $P4$ for design B are very similar to geometry A, but the value of $P3$ for geometry B is approximately equal to the value of $P3$ for geometry C.

Table 4.3. Geometric properties from selected Pareto Front individuals

Geometry	Nominal Case	A		B		C	
			% Change		% Change		% Change
m_{tot}/m_{nom}	1	0.61	-39.5	0.79	-21.2	3.22	222.0
$\omega_{pitch}/\omega_{pitch\ nom}$	1	1.08	8.3	0.44	-55.8	0.39	-61.0
Moonpool width (m)	30.9	43.78	41.7	42.45	37.4	11.34	-63.3
Hull width (m)	52.6	57.78	9.8	56.65	7.7	54.27	3.2
Heave plate width (m)	0	0.01	100.0	14.98	100.0	14.98	100.0
Hull height (m)	14.7	10.86	-26.1	11.16	-24.1	29.67	101.8
Draft (m)	11.6	8.86	-23.6	9.09	-21.6	22.58	94.7
Hull mass (kg)	2.04×10^7	1.19×10^7	-41.7	1.21×10^7	-40.7	6.42×10^7	214.7
Heave natural period (s)	10.1	8.31	-17.7	15.01	48.6	16.38	62.1
Pitch natural period (s)	11.6	11.05	-4.7	27.09	133.6	30.72	164.9

4.5. Discussion

Based on the results of Table 4.3, the mass ratio and pitch natural frequency do not have a significant dependence on the hull width ($P2$) as this value is approximately equal across all geometries. A smaller pitch natural frequency is achieved by increasing the draft of the system and decreasing the width of the moonpool. An additional trend in the results reveals that a relatively small sacrifice in the mass of the system can lead to a significant reduction in the pitch natural frequency as shown in the difference between designs A and B. This trend also exists in the other objective, as a small sacrifice in the pitch natural frequency leads to significant improvement in reducing the mass of the system when comparing designs C and B. Two of the three selected geometries make use of a heave plate which the baseline case does not have. Even if the heave plate perimeter is neglected the footprints of each of the selected geometries are larger than the baseline case. The mass of the hull for the baseline case (2.04×10^7 kg) is larger than that of either geometry A or geometry B, suggesting that despite their larger footprints they may be able to provide some material savings. The mass of geometry C suggests that the small advantage in pitch natural frequency would not be worth the sacrifice in mass.

Although these objective functions are important to the optimization of a wind turbine hull, there are many other aspects to consider. This optimization assumes that obtaining shorter platform pitch frequencies will yield better dynamic results, but this does not necessarily reflect optimal designs which include the potential motion reductions obtained from the moonpool effect for commonly occurring sea states with wave periods between 5 and 20 seconds. Further exploration of geometric complexity such as optimization of the shapes of the outer and moonpool perimeters could also have

an impact on the performance of the model. Another factor to look into would be the positioning of the heave plates in the vertical direction as well as their orientation.

All calculations have assumed a smeared density of the hull. In practice the density of the hull would not likely be uniform as the ballast (often water) would not completely fill the cavity of the hull. Additionally, it would be possible to utilize an active ballast system or to concentrate the ballast in particular regions within the hull to reduce dynamic system responses. Structural considerations for the system would also cause the need for supports to reduce the effective length of the structural members. Material selection would further dictate the variability of the density of the hull. Overall, the pitch performance and system can be improved with the selection of geometry B.

CHAPTER 5

CONCLUSIONS AND FUTURE WORK

5.1. Conclusions

A testing program was developed to validate the ability of ANSYS AQWA to model annular FOWT hulls with moonpools. A 1/100th-scale model of an annular hull was tested in the W2 basin which provided adequate results for comparison. Additionally, the annular hull was put into context in a comparison with other commercially available FOWT hull technologies.

Based on the results from this testing and validation effort, the following observations were made:

- ANSYS AQWA can adequately capture the impacts of moonpools in numerical modeling provided that the lid damping factor is properly tuned along with external damping
- The RAO magnitudes exhibited by the annular hull are generally higher than the results from the DeepCwind data set.

In this work, the general geometric shape was varied and the impacts on hydrodynamic performance were evaluated. The results of this work illustrate that a minimal sacrifice in the pitch RAO is likely worth the reduction in manufacturing and transportation complexity offered by the annular square hull. The comparison of geometric shape also confirmed that the moonpool does impact system motions in a positive way and allows for significant material reduction when comparing with a barge system for the support of a 6-MW turbine.

Further explorations in geometric variation led to an optimization of the square annular hull which expressed the wide range of hull heights and heave plate addition potential. Optimization results revealed that improvement in pitch performance from the baseline case is reliant on the addition of heave plates. Interestingly the width of the plates resulting from the optimization process exceeded the dimensions as described when considering the 6-MW-scale Ideol model. In addition to the necessity of heave plates for improved performance it was also noted that a significant increase in system draft to optimize for pitch natural frequency is not worth the sacrifice in system mass.

5.2. Future Work

All portions of this work assume a solid hull with uniform density which is a simplification when comparing to practical applications. Future work should include considering the potential variability in material selection for the structure itself as well as the ballast. Along with considering potential materials for the hull, the mooring method should also be taken into account when evaluating system responses. A hull with a catenary chain mooring system could experience significantly different mooring stiffnesses from a taught synthetic system—either of which would provide more than the zero magnitude pitch mooring stiffness case which is considered herein.

It is important to emphasize that this work only investigates unidirectional waves. With the motion of the water in the moonpool highly dependent on the motion of the water surrounding the hull the consideration of the multidirectional case would prove crucial for further development. Waves have only been assumed to approach from the direction perpendicular to the sides of the hull while interactions at an angle may have a significant impact in the motions of the water in the moonpool.

The applications for the annular FOWT hull as studied are rather limited as significant system responses are exhibited in the range of wave periods which represent typical sea states. Fortunately, significant potential exists for hull improvement for seaworthiness. Variability of geometry both along the perimeter of the hull as well as the perimeter of the moonpool could prove beneficial. Along with this, considerations for heave plate orientation including vertical positioning as well as the potential for angled heave plates may prove interesting. In these explorations it is important to remember that the FOWT industry is constantly evolving to support larger wind turbines so any solution should take scalability into consideration.

REFERENCES

- Aalbers, A. B. (1984). THE WATER MOTIONS IN A MOONPOOL. *Ocean Engng*, 11(6), 55–579. Retrieved from https://ac-els-cdn-com.prxy4.ursus.maine.edu/0029801884900015/1-s2.0-0029801884900015-main.pdf?_tid=f4ca800a-a842-11e7-be12-00000aab0f01&acdnat=1507039298_a8126e6063a77052a965a1a0545685b0
- ANSYS Inc. (2013a). Aqwa Theory Manual, 15317(November), 724–746.
- ANSYS Inc. (2013b). Aqwa User’s Manual. Canonsburg, PA: ANSYS, Inc.
- Beyer, F., Choisnet, T., Kretschmer, M., & Cheng, P. W. (2015). Coupled MBS-CFD Simulation of the IDEOL Floating Offshore Wind Turbine Foundation Compared to Wave Tank Model Test Data. In *International and Polar Engineering Conference*. International Society of Offshore and Polar Engineers. Retrieved from <https://www-onepetro-org.prxy4.ursus.maine.edu/download/conference-paper/ISOPE-I-15-272?id=conference-paper%2FISOPE-I-15-272>
- Chakrabarti, S. K. (1994). *Advanced Series on Ocean Engineering, Volume 9: Offshore Structure modeling*. World Scientific.
- Coulling, A. J., Goupee, A. J., Robertson, A. N., & Jonkman, J. M. (2013). IMPORTANCE OF SECOND-ORDER DIFFERENCE-FREQUENCY WAVE-DIFFRACTION FORCES IN THE VALIDATION OF A FAST SEMI-SUBMERSIBLE FLOATING WIND TURBINE MODEL, 1–10.
- Dagher, H., Viselli, A., Goupee, A., Kimball, R., & Allen, C. (2017). *The VoltturnUS 1:8 Floating Wind Turbine: Design, Construction, Deployment, Testing, Retrieval, and Inspection of the First Grid-Connected Offshore Wind Turbine in US*. Retrieved from <https://www.osti.gov/servlets/purl/1375022>
- Deb, K., Agrawal, S., Pratap, A., & Meyarivan, T. (2000). A Fast Elitist Non-Dominated Sorting Genetic Algorithm for Multi-Objective Optimization: NSGA-II. Retrieved from <http://www.iitk.ac.in/kangal>
- Det Norske Veritas. (2014). *Recommended Practice DNV-RP-C205: Environmental Conditions and Environmental Loads*. Retrieved from www.dnvgl.com.
- Dvorak, P. (2015). Denmark’s Henrik Stiesdal unveils open-sourced floating offshore platform. Can you improve on it? Retrieved May 23, 2018, from <https://www.windpowerengineering.com/business-news-projects/denmarks-henrik-stiesdal-unveils-open-sourced-floating-offshore-platform-can-you-improve-on-it/>
- Energias de Portugal. (2018). WindFloat | edp.com. Retrieved January 29, 2019, from <https://www.edp.com/en/windfloat>

- EOLFI. (2018). Les Eoliennes Flottantes de Groix & Belle-Ile Dossier D'information Septembre 2018. Retrieved from http://eoliennes-groix-belle-ile.com/wp-content/uploads/2018/10/eolfi_plaquette-12pages_13_bd.pdf
- Equinor. (2018). Hywind - leading floating offshore wind solution - equinor.com. Retrieved May 29, 2018, from <https://www.equinor.com/en/what-we-do/hywind-where-the-wind-takes-us.html>
- Fukushima Offshore Wind Consortium. (2013). *Fukushima Floating Offshore Wind Farm Demonstration Project (Fukushima FORWARD)*. Retrieved from <http://www.fukushima-forward.jp/english/pdf/pamphlet3.pdf>
- Fukushima Offshore Wind Consortium. (2016a). 5MW wind turbine on Fukushima Hamakaze being towed to off Fukushima coast / News / Fukushima Offshore Wind Consortium. Retrieved May 23, 2018, from http://www.fukushima-forward.jp/english/news_release/news160801.html
- Fukushima Offshore Wind Consortium. (2016b). *Fukushima Floating Offshore Wind Farm Demonstration Project (Fukushima FORWARD) - Construction of Phase II*. Retrieved from <http://www.fukushima-forward.jp>
- Gaillarde, G., & Cotteleer, A. (2005). WATER MOTION IN MOONPOOLS EMPIRICAL AND THEORETICAL APPROACH Anke COTTELEER. Maritime Research Institute, Netherlands. Retrieved from www.marin.nl
- GICON-SOF. (2015). Media: Das GICON®-SOF Schwimmendes Offshorefundament. Retrieved January 7, 2019, from <http://www.gicon-sof.de/en/media.html>
- GICON-SOF. (2018). Technical Solution: Das GICON®-SOF Schwimmendes Offshorefundament. Retrieved January 7, 2019, from <http://www.gicon-sof.de/en/technical-solution.html>
- Goupee, A. J., Koo, B. J., Kimball, R. W., Lambrakos, K. F., & Dagher, H. J. (2014). Experimental Comparison of Three Floating Wind Turbine Concepts. *Journal of Offshore Mechanics and Arctic Engineering*, 136(2), 020906. <https://doi.org/10.1115/1.4025804>
- Goupee, A. J., & Vel, S. S. (2007). Multi-objective optimization of functionally graded materials with temperature-dependent material properties. *Materials & Design*, 28(6), 1861–1879. <https://doi.org/10.1016/J.MATDES.2006.04.013>
- Greenovate! Europe EEIG. (2013). Floating offshore wind combining cost-competitiveness and high local content: Demonstration and benchmarking of a floating wind turbine system for power generation in Atlantic deep waters. Retrieved from http://ideol-offshore.com/sites/default/files/pdf/plaquette_floatgen-bd.pdf

- Großmann, J., Dahlhaus, F., Adam, F., & Schuldt, B. (2014). *The GICON®-TLP for wind turbines: Experimental Studies and numerical Modelling of structural Behavior of a Scaled Modular TLP Structure for Offshore Wind turbines*. Retrieved from https://www.sintef.no/globalassets/project/deepwind2014/presentations/e/adam-f_gicon.pdf
- GustoMSC. (2019). *TRI-FLOATER FLOATING OFFSHORE WIND TURBINE FOUNDATION*. Retrieved from www.gustomsc.com
- Halkyard, J. (2013). *Design and Analysis of Floating Structures*. (S. Chakrabarti, Ed.) (3rd, Versi ed.). Houston, TX: Elsevier Science.
- Hermans, K. W., Peeringa, J. M., & Verbruggen, T. (2016). *The influence of offshore floating foundations to the wind turbine generator A study using aNySIMPHATAS*. Retrieved from <https://www.ecn.nl/publications/PdfFetch.aspx?nr=ECN-E--16-032>
- Huijs, F., de Bruijn, R., & Savenije, F. (2014). Concept Design Verification of a Semi-submersible Floating Wind Turbine Using Coupled Simulations. *Energy Procedia*, 53, 2–12. <https://doi.org/10.1016/J.EGYPRO.2014.07.210>
- Ideol. (2018a). Floatgen is installed ! | Ideol. Retrieved January 7, 2019, from <https://www.ideol-offshore.com/en/actualites/floatgen-installed>
- Ideol. (2018b). Floating wind turbine solution | Japn offshore wind. Retrieved January 29, 2019, from <https://www.ideol-offshore.com/en/japanese-demonstrator>
- Ideol. (2018c). Ideol floating platform | offshore wind power. Retrieved December 28, 2018, from <https://www.ideol-offshore.com/en/floatgen-demonstrator>
- Jonkman, J. M. (2007). Dynamics Modeling and Loads Analysis of an Offshore Floating Wind Turbine Dynamics Modeling and Loads Analysis of an Offshore Floating Wind Turbine, (November).
- Koo, B. J., Goupee, A. J., Kimball, R. W., & Lambrakos, K. F. (2014). Model Tests for a Floating Wind Turbine on Three Different Floaters. *Journal of Offshore Mechanics and Arctic Engineering*, 136(2), 020907. <https://doi.org/10.1115/1.4024711>
- Kurtenbachap, E. (2013). Japan launches full-size floating wind turbine near Fukushima. *Portland Press Herald*. Retrieved from https://www.pressherald.com/2013/11/11/japan_launches_full-size_floating_wind_turbine_near_fukushima/

- Lauridsen, L. (2017). Millioner til Stiesdals flydende vindmølle-fundament | TV MIDTVEST. Retrieved May 23, 2018, from <https://www.tvmidtvest.dk/artikel/millioner-til-stiesdals-flydende-vindmoelle-fundament>
- LHEEA Centrale Nantes. (2018). FLOATGEN. cnrs. Retrieved from <https://lhea.ec-nantes.fr/partnerships-and-projects/research-projects/floatgen-201151.kjsp>
- Liu, Y., Li, S., Yi, Q., & Chen, D. (2016). Developments in semi-submersible floating foundations supporting wind turbines: A comprehensive review. *Renewable and Sustainable Energy Reviews*, 60, 433–449. <https://doi.org/10.1016/J.RSER.2016.01.109>
- Manzanas Ochagavia, R., Pascual Vergara Daniel Castell, J., Rodriguez Tsouroukdissian Jaco Korbijn, A., Bolleman Francisco J Huera-Huarte, N. C., Schuon, F., Ugarte Johan Sandberg Vincent de Laleu, A., ... Wilkes, J. (2013). *Deep Water The next step for offshore wind energy*. (J. S. and Sarah Azau, Stéphane Bourgeois, Zoë Casey, Jacopo Moccia, Vilma Radvilaite & Justin Wilkes (EWEA), Eds.). Retrieved from www.ewea.org/report/deep-water
- Mitsubishi Corporation. (2015). Fukushima Experimental Offshore Floating Wind Farm Project: Second Phase Update. Retrieved January 7, 2019, from <https://www.mitsubishicorp.com/jp/en/pr/archive/2015/html/0000027886.html>
- Molin, B. (2001). On the piston and sloshing modes in moonpools. *J. Fluid Mech*, 430, 27–50. <https://doi.org/10.1017/S0022112000002871>
- Musial, W. (2018). *Offshore Wind Resource, Cost, and Economic Potential in the State of Maine*. Retrieved from <https://www.nrel.gov/docs/fy18osti/70907.pdf>
- Musial, W., Heimiller, D., Beiter, P., Scott, G., & Draxl, C. (2016). *2016 Offshore Wind Energy Resource Assessment for the United States*. Retrieved from www.nrel.gov/publications.
- offshoreWIND.biz. (2016a). Fukushima Hamakaze Nearing Completion | Offshore Wind. Retrieved May 23, 2018, from <https://www.offshorewind.biz/2016/05/06/fukushima-hamakaze-nearing-completion/>
- offshoreWIND.biz. (2016b). Fukushima Hamakaze Spar Tilts Back Into Position | Offshore Wind. Retrieved May 23, 2018, from <https://www.offshorewind.biz/2016/05/17/fukushima-hamakaze-spar-tilts-back-into-position/>
- Principle. (2014). *WindFloat Pacific OSW Project*. Retrieved from <https://www.boem.gov/NREL-WindFloat-Pacific-OSW-Project/>

- Robertson, A. N., & Jonkman, J. M. (2011). *Loads Analysis of Several Offshore Floating Wind Turbine Concepts*. Retrieved from www.deepcwind.org
- Sclavounos, P. (2008). Floating Offshore Wind Turbines. *Marine Technology Society Journal*, 42(2), 39–43. <https://doi.org/10.4031/002533208786829151>
- Stehly, T., Beiter, P., Heimiller, D., & Scott, G. (2017). *2017 Cost of Wind Energy Review*. Retrieved from www.nrel.gov/publications.
- WINDEXchange. (2017). WINDEXchange: U.S. Wind Power Resource at 100-meter Hub Height. Retrieved August 22, 2018, from <https://windexchange.energy.gov/maps-data/324>

APPENDIX A: OPTIMIZATION MATLAB FUNCTIONS

```
%H. Allen
% Last updated 05/01/2019

function [obj1,obj2,c, kP, g1, g2, g3, g4] = myfuns(p)
%% Constants
g = 9.81; %%m/s^2
dh2o = 1025; %%density of sea water kg/m^3
dhull = 768.03;%%density of hull kg/m^3
dplate = 1895;%%density of heave plate kg/m^3
tplate = 0.457;%%heave plate thickness (~1.5ft)
mturb = 438*10^3; %%turbine mass, kg
mtow0 = 517.371*10^3; %%tower mass, kg
%mtt = mturb+mtow; %%Mass of turbine and tower, metric tons
towhgt0 = 83.5; %nominal tower height, m
towcgz0 = 36.3463; %nominal tower cg from base
wind = 846*10^3; %%Design case wind load, N
windarm = 100; %%moment arm for wind turbine, m
windmom = wind*windarm; %%wind moment
mnom = 21341.181*10^3; %%nominal mass of hull, turbine, tower, ballast
wheavenom = 0.625; %%nominal heave natural frequency, rad/s FIX!!!
wpitchnom = 0.525; %%nominal pitch natural frequency, rad/s FIX!!!
%%optimization, previously determined, kg
%% Design variable dependent calculations: p is the vector of
%design variables
moonside = p(1);%%p1=moonpool side length
hullside = p(2);%%p2=hull body side length
platew = p(3);%%p3=heave plate width
hullh = p(4); %%p4=hull height

Awp = (hullside^2-moonside^2);%%waterplane area, m
vhull = Awp*hullh; %%hull total volume, m^3
mhull = (vhull*dhull); %%mass of hull w/ballast
thull = (hullside-moonside)/2; %%thickness of hull

vplate = ((hullside+2*platew)^2-(hullside^2))*tplate; %plate volume
mplate = vplate*dplate; %%plate mass

%m = mhull+mplate+mtt; %%total system mass, kg

%%draft based on mass of system
draft = (mhull+mturb+mtow0*((100-hullh)/towhgt0))/...
        ((-mtow0/towhgt0)+dh2o*Awp);%draf, m
vsub = draft*Awp+vplate; %%submerged volume
towhgt = 100-(hullh-draft); %height of tower maintaining hub height of
100m
towcgz = towcgz0*(towhgt/towhgt0); %tower center of gravity
mtow = mtow0*(towhgt/towhgt0); %mass of tower
mtt = mturb+mtow; %% mass of turbine and tower, kg
m = mhull+mplate+mtt; %%total system mass, kg

%%CG in reference to water line at aft, left corner (behind turbine)
```

```

CGx = (hullside)/2; %location of center of gravity in surge direction,
m
CGy = CGx; %location of center of gravity in sway direction, m
%location of center of gravity in heave direction, m
CGz = ((mhull*((hullh/2)-draft))+(mplate*-(draft-(tplate/2)))...
+mturb*(100)+mtow*(towcgz+(hullh-draft)))/m;

%%Waterplane stiffness (P=pitch, H=heave)
kP = (dh2o*g*(hullside^4-moonside^4)/12)+(dh2o*g*vsub*-draft/2)-
(m*g*CGz);%Nm/rad
kH = (dh2o*g*(hullside^2-moonside^2)); %N/m

thetaP = (windmom/kP)*(360/2*pi); %%pitch rotation, degrees

%%Pitch Inertia (values for added mass calculated later on)
IPplate =
(mplate/2)*(((hullside+2*platew)^2)/12)+(((hullside+platew)/2)^2));
%plate inertia
IPhull = (mhull - mtt)/2*(((hullside^2)/12)+((hullside-thull)/2)^2);
%hull inertia
%Inertia due to counterweight to balance turbine and tower,
%positioned in hull horizontally 180 degrees from turbine and tower.
IPthull = mtt*((hullside/2)^2);
%turbine and tower inertia, assuming cg is at MWL
IPtt = (mturb*(100^2)+mtow*((towcgz+(hullh-draft))^2));
IP = IPplate+IPhull+IPthull+IPtt;
%% Constraint functions. All nom values are based on the nominal 6MW
hull
%%g1 constraint of width of hull segment
tnom = 10.823; %%nominal thickness of hull segment, m
if thull<=7
    g1 = (7-thull)/tnom;
else
    g1 = 0;
end

%%g2 drives draft to be less than hull height (bouyancy)
dnom = 11.596; %%m
if draft>=hullh
    g2 = (draft-hullh)/dnom;
else
    g2 = 0;
end

%%g3 drives pitch stiffness to be as good or better than the nominal
case
kPnom = 4630990675; %%Nm/rad
if kP<=0
    g3 = -kP/kPnom;
else
    g3 = 0;
end

%%g4 drives pitch angular displacement to be less than or equal to the

```

```

%%nominal case
thetaPnom = 0.018269*(360/2*pi); %%nominal pitch angular disp, deg
thetamax = 10; %deg
if thetaP>=thetamax
    g4 = (thetaP-thetamax)/thetamax;
else
    g4 = 0;
end

%%g5 (added 3-5-19) drives the freeboard of the hull to be 2 m or
%%greater to help reduce greenwater in day-to-day conditions
minfreeb = 2; % minimum freeboard, m
freeb = hullh-draft;
if freeb<=minfreeb
    g5 = (minfreeb-freeb)/minfreeb;
else
    g5 = 0;
end

c = g1+g2+g3+g4+g5;

%% Calculate objective functions
if (c <= 0)

    %%added masses in heave based on DNV-RP-C205 2-D guidelines
    %%HEAVE FROM HULL%%
    ratio = ((hullside-moonside)/2)/draft;
    if ratio>10.5
        CA = 1;
    elseif (ratio>=7.5) && (ratio<=10.5)
        CA = 1.14;
    elseif (ratio>=3) && (ratio<7.5)
        CA = 1.21;
    elseif (ratio>=1.5) && (ratio<3)
        CA = 1.36;
    elseif (ratio>=0.75) && (ratio<1.5)
        CA = 1.51;
    elseif (ratio>=0.35) && (ratio<0.75)
        CA = 1.70;
    elseif (ratio>=0.15) && (ratio<0.35)
        CA = 1.98;
    % elseif (ratio>=.085) && (ratio<0.15)
    %     CA = 2.23;
    elseif (ratio == 0)
        CA = 0;
    else
        CA = 2.23;
    end
    AR = pi*(((hullside-moonside)/4)^2); %reference area as defined by
C205
    L = 4*(hullside-((hullside-moonside)/2)); %sidelengths relevant to
hull heave
    maddedHh = dh2o*CA*AR; %hull heave added mass per length
    maddedHhtot = L*dh2o*CA*AR;

    %%HEAVE FROM HEAVE PLATES%%

```

```

ratio = platew/tplate;
    if ratio>10.5
        CA = 1;
    elseif (ratio>=7.5) && (ratio<=10.5)
        CA = 1.14;
    elseif (ratio>=3) && (ratio<7.5)
        CA = 1.21;
    elseif (ratio>=1.5) && (ratio<3)
        CA = 1.36;
    elseif (ratio>=0.75) && (ratio<1.5)
        CA = 1.51;
    elseif (ratio>=0.35) && (ratio<0.75)
        CA = 1.70;
    elseif (ratio>=0.15) && (ratio<0.35)
        CA = 1.98;
    else
        CA = 2.23;
    end
AR = pi*(platew/2)^2;
L = 4*(hullside+platew);%sidelengths relevant to plate heave
maddedHp = dh2o*CA*AR; %plate heave added mass per unit length
maddedHptot = L*dh2o*CA*AR;%updated 1-25 to reflect 4 plate
segments

maddedHtot= maddedHhtot+maddedHptot; %total added mass in heave, kg
wheave = sqrt(kH/(m+maddedHtot));%heave natural frequency
critdamp =2*sqrt(kH*(m+maddedHtot)); %critical damping
critdampH = 0.1*critdamp; %10% of critical damping

%% added mass inertia in pitch based on heave added mass from
% DNV-RP-C205
%FROM HULL%
IaddedPh = (2*maddedHh*hullside*((hullside/2)-
(thull/2))^2)+(2*(1/12)*maddedHh*moonside*(moonside^2));%%added
inertia (kgm^2)from hull
%FROM PLATE%
IaddedPp =
(2*maddedHp*(hullside+2*platew)*((hullside+2*platew)/2)^2)+(2*(1/12)*ma
ddedHp*(hullside+2*platew)*((hullside+2*platew)^2));; %%pitch added
inertia from plates

IaddedP = IaddedPh+IaddedPp;%total pitch inertia
wpitch = sqrt(kP/(IP+IaddedP));
%wpitch = 2*pi/wpitch; %%pitch natural period, s

%Objective Functions
obj1 = -m/mnom; %normalized mass, trying to minimize

obj2 = -sqrt(kP/(IP+IaddedP))/wpitchnom;
%%normalized pitch natural frequency, trying to minimize
else
    obj1 = -(5+c);
    obj2 = -(5+c);
end

%Main Multi-Objective Genetic Algorithm (MOGA) Input Page

```

```

%Andrew Goupee
%Last modified: 12-2-04

%This algorithm utilizes an elitist multi-objective genetic algorithm
with
%crowded tournament selection and a constrained non-domination sorting
%routine. Details of these operators can be viewed in Deb's book.
%This m-file allows one to select the values of various MOGA parameters
used
%in searching for the pareto-optimal front (searching for maximums)
under
%linear and/or %nonlinear constraints. Recommended values of the GA
parameters
%are given in various works by Deb. The parameters to be chosen are as
%follows:

%MOGA parameters to be chosen:
%max_gen - the number of generations until termination
%n_pop - size of GA population (must be an even number)
%n_genes - number of genes in an individuals chromosome
%ub_1 - vector of upper bounds on genes (design parameters) for initial
% population, dimensions of 1 row x n_genes columns
%lb_1 - vector of lower bounds on genes (design parameters) for initial
% population, dimensions of 1 row x n_genes columns
%ub_2 - vector of upper bounds on genes (design parameters) for all
% populations after initial, dimensions of 1 row x n_genes columns
%lb_2 - vector of lower bounds on genes (design parameters) for all
% populations after initial, dimensions of 1 row x n_genes columns
%pc - probability of crossover per pair of parents
%pcg - probability of crossover per gene
%nc - crossover strength parameter (smaller values increase strength)
%pm - probability of mutation per individual
%pmg - probability of of mutation per gene
%nm - mutation strength parameter (smaller values increase strength)
%drop - overall percent reduction in chosen parameters (for those that
% apply) calculated during dynamic parameter alteration
%dyn - strength parameter for dynamic alteration scheme (larger values
% reduce parameters by percent allotted in 'drop' quicker)
%objective1, objective2 - character strings containing the names of the
% two objective functions to be maximized
%constraint - character string containing the name of the constraint
% function

%Output
%A plot of the fitness functions

clear all;

%Select GA paramters:
max_gen = 100; %Number of generations

n_pop = 100; %Number of members of each population

n_genes = 4; %Number of variables to be manipulated

```

```

ub_1 = [60 74 15 30]; %Upper bounds on genes in meters, applied
throughout

lb_1 = [10 30 0 5]; %Lower bounds on genes in meters, applied
throughout

ub_2 = ub_1;

lb_2 = lb_1;

pc = 1;

pcg = .5;

nc = 2;

pm = .1;

pmg = .5;

nm = 2;

plotbounds=[0 2.5 0 1];

track=0;

minplot=1;

%Provide objective and constraint function name
objective = 'myfuncs';

%Perform GA search and optimization
[population]=MOGAMain(max_gen,n_pop,n_genes,ub_1,lb_1,ub_2,lb_2,...
    pc,pcg,nc,pm,pmg,nm,objective,...
    plotbounds,track,minplot);

```

```

function [population] =
MOGAmainMOGAmain(max_gen,n_pop,n_genes,ub_1,lb_1,...
ub_2,lb_2,pc,pcg,nc,pm,pmg,nm,objective,...
plotbounds,track,minplot)
%Main multi-objective genetic algorithm program
%Andrew Goupee
%Last modified: 12-02-4

%Initialize generation number, corresponding generation
generation = 0;
[population] = create_population(n_pop,n_genes,ub_1,lb_1,objective);

pause(0.01);
figure(1);
clf;
hold on;
axis(plotbounds);
title('Generation 0');
if (minplot == 1)
    for i=1:n_pop
        plot(-population(i,4),-population(i,5),'k.');
```

```

        if (track == 1)
            stores(i,2*generation+1)=-population(i,4);
            stores(i,2*generation+2)=-population(i,5);
        end;
    end;
else
    for i=1:n_pop
        plot(population(i,4),population(i,5),'k.');
```

```

        if (track == 1)
            stores(i,2*generation+1)=population(i,4);
            stores(i,2*generation+2)=population(i,5);
        end;
    end;
end;
pause(0.01);

%Begin looping through generations
generation = 1;
while (generation <= max_gen)

    %Perform tournament selection
    [population] = matingpool(population);

    %Perform crossover and mutation to create 2N mating pool
    [dpop] = hankypanky(population,pc,pcg,pm,pmg,ub_2,lb_2,...
nc,nm,objective);

    %Perform elitist function
    population = dpop(1:n_pop,:);

    pause(0.01);
    figure(1);
    if (track == 0)
        clf;

```

```

hold on;
axis(plotbounds);
title(['Generation ', num2str(generation)]);
if (minplot == 1)
    for i=1:n_pop
        plot(-population(i,4), -population(i,5), 'k. ');
    end;
else
    for i=1:n_pop
        plot(population(i,4), population(i,5), 'k. ');
    end;
end;
else
    clf;
hold on;
axis(plotbounds);
title(['Generation ', num2str(generation)]);
if (minplot == 1)
    for i=1:n_pop
        for j=1:generation
            plot(stores(i,2*j-1), stores(i,2*j), 'mo');
            plot(stores(i,2*j-1), stores(i,2*j), 'mo');
        end;
    end;
    for i=1:n_pop
        plot(-population(i,4), -population(i,5), 'k. ');
        stores(i,2*generation+1)=-population(i,4);
        stores(i,2*generation+2)=-population(i,5);
    end;
else
    for i=1:n_pop
        for j=1:generation
            plot(stores(i,2*j-1), stores(i,2*j), 'mo');
            plot(stores(i,2*j-1), stores(i,2*j), 'mo');
        end;
    end;
    for i=1:n_pop
        plot(population(i,4), population(i,5), 'k. ');
        stores(i,2*generation+1)=population(i,4);
        stores(i,2*generation+2)=population(i,5);
    end;
end;
end;
end;
pause(0.01);

%Count up generation
generation = generation + 1;

%Save GA information
save moga_info;

population(:,4:5)
end;

```

```

function [population] = create_population(n_pop,n_genes,ub_1,lb_1,...
    objective)
%Initial population creator
%Andrew Goupee
%Last modified: 12-2-04

%This is a multi-objective population creator routine.

%Reset random number generator
rand('state',sum(100*clock));

%Size population
population = zeros(n_pop,(n_genes+6));

%Create genes values
for i = 1:n_pop
    for j = 7:(n_genes+6)
        population(i,j) = (rand*(ub_1(j-6)-lb_1(j-6)))+lb_1(j-6);
    end;
end;

%Fill in ID#/workspace, objective functions 1 and 2, constraint
for i = 1:n_pop
    population(i,1) = 0;
    [o1,o2,con]=feval(objective,(population(i,7:(n_genes+6))));
    population(i,4) = o1;
    population(i,5) = o2;
    population(i,6) = con;
end;

%Determine non-dominated sorting
[population] = rankassign(population);

%Determine crowding distance
[population] = crowdassign(population);

```

```

function [matepool] = matingpool(population)
%This creates a mating pool from a population
%Andrew Goupee
%12-03-04

population(:,1)=0;
[n_pop,len]=size(population);
matepool=zeros(n_pop,len);

for i=1:n_pop

    %Select individual 1
    flag=0;
    while (flag < 1)
        no_1=random(n_pop);
        if (population(no_1,1) < 2)
            dud1=population(no_1,:);
            flag=1;
            population(no_1,1)=population(no_1,1)+1;
        end;
    end;

    %Select individual 2
    flag=0;
    while(flag < 1)
        no_2=random(n_pop);
        if (population(no_2,1) < 2)
            dude2=population(no_2,:);
            flag=1;
            population(no_2,1)=population(no_2,1)+1;
        end;
    end;

    %Conduct tournament
    if (dud1(1,2) < dude2(1,2))
        matepool(i,:)=dud1;
    elseif (dude2(1,2) < dud1(1,2))
        matepool(i,:)=dude2;
    else
        if (dud1(1,3) > dude2(1,3))
            matepool(i,:)=dud1;
        elseif (dude2(1,3) > dud1(1,3))
            matepool(i,:)=dude2;
        else
            matepool(i,:)=dud1;
        end;
    end;

end;

matepool(:,1)=0;

```

```

function [dpop] = crossmutate(population,pc,pcg,pm,pmg,ub_2,lb_2,...
    nc,nm,objective)
%This function performs crossover, mutation, makes 2N population
%Andrew Goupee
%Last modified: 12-03-04

population(:,1)=0;
[n_pop,len]=size(population);
dpop=zeros(2*n_pop,len);
dpop(1:n_pop,:)=population;
dpop(:,1:3)=0;
n_genes=len-6;

%Make children
for i=1:(n_pop/2)

    checks=[0 0];

    %Pick out mom
    flag=0;
    while (flag < 1)
        no_1=random(n_pop);
        if (dpop(no_1,1) < 1)
            parent_1 = dpop(no_1,:);
            dpop(no_1,1)=1;
            flag=1;
        end
    end

    %pick out dad
    flag=0;
    while (flag < 1)
        no_2=random(n_pop);
        if (dpop(no_2,1) < 1)
            parent_2 = dpop(no_2,:);
            dpop(no_2,1)=1;

            flag=1;
        end
    end

    %Perform crossover if necessary
    if (rand <= pc)

        checks = [1 1];

        %Loop through genes
        for j = 7:(n_genes+6)

            %Determine if genes are to be crossed
            if (rand <= pcg)

                %Perform crossover
                if (parent_1(1,j) < parent_2(1,j))
                    x1 = parent_1(1,j);

```

```

        x2 = parent_2(1,j);
    else
        x1 = parent_2(1,j);
        x2 = parent_1(1,j);
    end

    if (x2 == x1)
        difference = .01;
    else
        difference = x2 - x1;
    end

    beta = 1 + (2/difference)*...
        (min([(x1-lb_2(1,j-6)), (ub_2(1,j-6)-x2)]));

    alpha = 2 - beta^(-(nc+1));

    u = rand;
    if (u <= (1/alpha))
        beta_bar = (alpha*u)^(1/(nc+1));
    else
        beta_bar = (1/(2-alpha*u))^(1/(nc+1));
    end

    y1 = 0.5*((x1+x2) - beta_bar*(x2-x1));
    y2 = 0.5*((x1+x2) + beta_bar*(x2-x1));

    if (parent_1(1,j) < parent_2(1,j))
        child_1(1,j) = y1;
        child_2(1,j) = y2;
    else
        child_1(1,j) = y2;
        child_2(1,j) = y1;
    end
end
else
    child_1(1,j) = parent_1(1,j);
    child_2(1,j) = parent_2(1,j);
end
end
else
    %Just copy over parents to children if no crossover at all
    child_1 = parent_1;
    child_2 = parent_2;
end
%Mutate if necessary
%child_1
if (rand < pm)

    checks(1,1) = 1;

    %Erase fitness and constraint violation
    child_1(1,1:6)=0;

    %Loop through genes
    for j=7:(n_genes+6)

```

```

%Determine if gene is to be mutated
if (rand < pmg)

    %Perform mutation
    x = child_1(1,j);

    %Calculate gap
    if (ub_2(1,j-6) == lb_2(1,j-6))
        gap = 1;
    else
        gap = ub_2(1,j-6)-lb_2(1,j-6);
    end

    delta = (min([(x-lb_2(1,j-6)), (ub_2(1,j-6)-x)]))/...
        gap;

    u = rand;
    if (u <= 0.5)
        delta_bar = ((2*u+(1-2*u))*((1-delta)^(nm+1)))...
            ^ (1/(nm+1)) - 1;
    else
        delta_bar = 1 - (2*(1-u)+2*(u-0.5))*((1-
delta)^(nm+1)))...
            ^ (1/(nm+1));
    end

    y = x + delta_bar*(ub_2(1,j-6) - lb_2(1,j-6));

    child_1(1,j) = y;
end
end
end

%child_2
if (rand < pm)

    checks(1,2) = 1;

    %Erase fitness and constraint violation
    child_2(1,1:6)=0;

    %Loop through genes
    for j=7:(n_genes+6)

        %Determine if gene is to be mutated
        if (rand < pmg)

            %Perform mutation
            x = child_2(1,j);

            %Calculate gap
            if (ub_2(1,j-6) == lb_2(1,j-6))
                gap = 1;
            end
        end
    end
end

```

```

        else
            gap = ub_2(1,j-6)-lb_2(1,j-6);
        end

        delta = (min([(x-lb_2(1,j-6)), (ub_2(1,j-6)-x)]))/...
            gap;

        u = rand;
        if (u <= 0.5)
            delta_bar = ((2*u+(1-2*u))*((1-delta)^(nm+1)))...
                ^(1/(nm+1)) - 1;
        else
            delta_bar = 1 - (2*(1-u)+2*(u-0.5))*((1-
delta)^(nm+1)))...
                ^(1/(nm+1));
        end

        y = x + delta_bar*(ub_2(1,j-6) - lb_2(1,j-6));

        child_2(1,j) = y;
    end
end

dpop((2*i)-1+n_pop,:)=child_1;
dpop(2*i+n_pop,:)=child_2;

%Evaluate objective function if needed
if (checks(1,1) == 0)
    dpop((2*i)-1+n_pop,4)=parent_1(1,4);
    dpop((2*i)-1+n_pop,5)=parent_1(1,5);
    dpop((2*i)-1+n_pop,6)=parent_1(1,6);
else
    [o1,o2,con]=feval(objective,(child_1(1,7:(n_genes+6))));
    dpop((2*i)-1+n_pop,4)=o1;
    dpop((2*i)-1+n_pop,5)=o2;
    dpop((2*i)-1+n_pop,6)=con;
end

if (checks(1,2) == 0)
    dpop(2*i+n_pop,4)=parent_2(1,4);
    dpop(2*i+n_pop,5)=parent_2(1,5);
    dpop(2*i+n_pop,6)=parent_2(1,6);
else
    [o1,o2,con]=feval(objective,(child_2(1,7:(n_genes+6))));
    dpop(2*i+n_pop,4)=o1;
    dpop(2*i+n_pop,5)=o2;
    dpop(2*i+n_pop,6)=con;
end

end
end
%Rank assign
[dpop] = rankassign(dpop);

%Crowd assign
[dpop] = crowdassign(dpop)

```

```

function [popranked] = rankassign(population)
%Rank assignment routine
%Andrew Goupee
%Last modified: 12-3-04
%This routine takes in a population of size n_pop and
%finds their non-dominant rank and assigns it

[n_pop,len]=size(population);
n_genes=len-6;

remainder=population;
remainder(1:n_pop,1:3)=0;
[n_rem,soup]=size(remainder);
population=zeros(n_pop,(n_genes+6));

count=1;
rank=1;

while (count <= n_pop)

    for i=1:n_rem
        for j=1:n_rem
            [flag]=dominate(remainder(j,:),remainder(i,:));
            remainder(i,1)=remainder(i,1)+flag;
        end;
    end;

    rcount=1;

    for i=1:n_rem
        if (remainder(i,1) == 0)
            population(count,:)=remainder(i,:);
            population(count,2)=rank;
            count=count+1;
        else
            remainder2(rcount,:)=remainder(i,:);
            rcount=rcount+1;
        end;
    end;

    if (rcount > 1)
        remainder2=remainder2(1:rcount-1,:);
    else
        remainder2=remainder2(1,:);
    end;

    [n_rem,soup]=size(remainder2);
    remainder=remainder2;
    remainder(:,1)=0;
    rank=rank+1;

end;

popranked=population(1:n_pop,:);
function [popcrowd] = crowdassign(population)

```

```

%Crowding distance assignment routine
%Andrew Goupee
%Last modified: 12-3-04

[n_pop, len]=size(population);

%Finds ranks and rankcol
population(:,3)=0;
ranks=1;
rankcol=zeros(population(n_pop,2),1);
for i=1:n_pop
    if (population(i,2) == ranks)
        rankcol(ranks,1)=rankcol(ranks,1)+1;
    else
        ranks=ranks+1;
        rankcol(ranks,1)=rankcol(ranks,1)+1;
    end;
end;

%Sorts in descending order for objective function 1
start=1;
for i=1:ranks
    pop2=population(start:start+rankcol(i,1)-1,:);
    pop2=sortrows(pop2,4);
    pop3=zeros(rankcol(i,1),len);
    for j=1:rankcol(i,1)
        pop3(j,:)=pop2((rankcol(i,1)-j+1),:);
    end;
    population(start:start+rankcol(i,1)-1,:)=pop3;
    start=start+rankcol(i,1);
end;

%Calculates contribution to di from objective function 1
start=0;
for i=1:ranks
    for j=1:rankcol(i,1)
        if (j == 1)
            population(start+j,3)=population(start+j,3)+10e6;
        elseif (j == rankcol(i,1))
            population(start+j,3)=population(start+j,3)+10e6;
        else
            if (population(start+1,4) ==
population(start+rankcol(i,1),4))
                gap=1;
            else
                gap=(population(start+1,4)-
population(start+rankcol(i,1),4));
            end;
            population(start+j,3)=population(start+j,3)+...
(population(start+j-1,4)-
population(start+j+1,4))/gap;...
        end;
    end;
    start=start+rankcol(i,1);
end;

```

```

%Sorts in descending order for objective function 2
start=1;
for i=1:ranks
    pop2=population(start:start+rankcol(i,1)-1,:);
    pop2=sortrows(pop2,5);
    pop3=zeros(rankcol(i,1),len);
    for j=1:rankcol(i,1)
        pop3(j,:)=pop2((rankcol(i,1)-j+1),:);
    end;
    population(start:start+rankcol(i,1)-1,:)=pop3;
    start=start+rankcol(i,1);
end;

%Calculates contribution to di from objective function 2
start=0;
for i=1:ranks
    for j=1:rankcol(i,1)
        if (j == 1)
            population(start+j,3)=population(start+j,3)+10e6;
        elseif (j == rankcol(i,1))
            population(start+j,3)=population(start+j,3)+10e6;
        else
            if (population(start+1,5) ==
population(start+rankcol(i,1),5))
                gap=1;
            else
                gap=(population(start+1,5)-
population(start+rankcol(i,1),5));
            end;
            population(start+j,3)=population(start+j,3)+...
(population(start+j-1,5)-
population(start+j+1,5))/gap;...
        end;
    end;
    start=start+rankcol(i,1);
end;

%Sorts by crowding distance in descending order
start=1;
for i=1:ranks
    pop2=population(start:start+rankcol(i,1)-1,:);
    pop2=sortrows(pop2,3);
    pop3=zeros(rankcol(i,1),len);
    for j=1:rankcol(i,1)
        pop3(j,:)=pop2((rankcol(i,1)-j+1),:);
    end;
    population(start:start+rankcol(i,1)-1,:)=pop3;
    start=start+rankcol(i,1);
end;

popcrowd=population;

```

```
function [number] = random(n)
%Random number generator
%Andrew Goupee
%Last modified: 4-21-04

%This function generates a random integer between 1 and n (an
%integer value) and places that value in number (the output).

%Create random number
number = round((n)*rand(1)+0.5);

%Ensure a reasonable number
if number < 1;
    number = 1;
elseif number > n;
    number = n;
else;
    %nothing new happens
end;
```

```

function [flag] = dominate(dudel1,dude2)
%Andrew Goupee
%12-2-04

%Asks the question, and answers, does dudel1 dominate dude2?
%flag = 1 is yes
%flag = 0 is no

flag = 0;

if ((dudel1(1,6) == 0) && (dude2(1,6) > 0))
    flag = 1;
end

if ((dudel1(1,6) > 0) && (dude2(1,6) > 0) && (dudel1(1,6) < dude2(1,6)))
    flag=1;
end

if ((dudel1(1,6) == 0) && (dude2(1,6) == 0))
    if ((dudel1(1,4) >= dude2(1,4)) && (dudel1(1,5) >= dude2(1,5)))
        flag=1;
    end
end

if ((dudel1(1,4) == dude2(1,4)) && (dudel1(1,5) == dude2(1,5)))
    flag = 0;
end

```

APPENDIX B: OPTIMIZATION GENERATION 100 POPULATION

Table B.1. Generation 100 Population

Mass Ratio	Pitch Frequency Ratio	Constraint Function	P1	P2	P3	P4
0.6048	1.0826	0.0000	43.7763	57.7769	0.0102	10.8611
3.2229	0.3895	0.0000	11.3429	54.2658	14.9860	29.6697
1.7698	0.4009	0.0000	43.9677	58.0237	14.9936	29.9379
2.4625	0.4007	0.0000	28.0646	54.0795	14.9873	29.2163
0.9322	0.4356	0.0000	42.4540	56.6538	14.9826	14.0044
0.6372	1.0173	0.0000	43.7858	57.7869	3.3318	10.8465
2.9550	0.3922	0.0000	19.9865	54.2225	14.9909	29.9571
3.1408	0.3921	0.0000	14.4126	54.2684	14.9817	29.6905
1.5876	0.4123	0.0000	43.9677	58.0299	14.9878	26.3882
1.1966	0.4321	0.0000	43.8336	57.8540	14.9894	18.9240
1.0154	0.4323	0.0000	42.6967	56.7249	14.9582	15.7942
1.4449	0.4225	0.0000	44.0176	58.0291	14.9505	23.7040
2.5626	0.3980	0.0000	27.6294	54.2225	14.9860	29.9571
2.7339	0.3965	0.0000	24.5597	54.2257	14.9887	29.9363
0.7102	0.7023	0.0000	43.7749	57.7849	9.5474	10.8761
0.7185	0.6601	0.0000	43.7380	57.7413	10.3011	10.8666
0.7885	0.4417	0.0000	42.4540	56.6538	14.9826	11.1616
0.6476	0.9777	0.0000	43.7858	57.7862	4.3451	10.8405
0.6761	0.8627	0.0000	43.7714	57.7721	6.7768	10.8687
0.6864	0.8128	0.0000	43.7709	57.7771	7.6403	10.8684
0.7259	0.6336	0.0000	43.7604	57.7742	10.8040	10.8701
0.6970	0.7666	0.0000	43.7712	57.8006	8.4360	10.8684
2.8340	0.3942	0.0000	21.6761	54.0438	14.9779	29.6891
0.6636	0.9192	0.0000	43.7738	57.7781	5.7591	10.8478
0.6700	0.8907	0.0000	43.7266	57.7377	6.2730	10.8652
0.6996	0.7479	0.0000	43.7749	57.7759	8.7490	10.8697
0.6700	0.8907	0.0000	43.7266	57.7377	6.2730	10.8652
0.7302	0.6162	0.0000	43.7600	57.7742	11.1410	10.8701
0.7361	0.5898	0.0000	43.7293	57.7413	11.6607	10.8613
1.6750	0.4077	0.0000	43.9677	58.0697	14.9936	27.9908
0.7456	0.5543	0.0000	43.7295	57.7353	12.3993	10.8613
0.7391	0.5788	0.0000	43.7356	57.7413	11.8829	10.8669
0.6615	0.9369	0.0000	43.7281	57.7609	5.4125	10.8688
0.6539	0.9605	0.0000	43.7268	57.7618	4.6874	10.8737
0.7020	0.7356	0.0000	43.7723	57.7744	8.9620	10.8651

Table B.1. Continued

Mass Ratio	Pitch Frequency Ratio	Constraint Function	P1	P2	P3	P4
1.0154	0.4324	0.0000	42.6967	56.7249	14.9548	15.7942
1.2218	0.4309	0.0000	43.8284	57.8540	14.9915	19.4105
3.2127	0.3903	0.0000	11.3429	54.2715	14.9845	29.5627
1.6406	0.4091	0.0000	43.9677	58.0340	14.9936	27.4057
0.7514	0.5353	0.0000	43.6938	57.6969	12.8087	10.8789
0.7580	0.5131	0.0000	43.7305	57.7334	13.3249	10.8618
0.6787	0.8562	0.0000	43.7750	57.8023	6.8997	10.8677
1.3268	0.4276	0.0000	43.8136	57.8417	14.9383	21.4748
0.7768	0.4586	0.0000	43.7288	57.7321	14.6889	10.8566
0.7075	0.7141	0.0000	43.7805	57.7849	9.3372	10.8768
0.6935	0.7783	0.0000	43.7667	57.7725	8.2268	10.8704
0.6219	1.0631	0.0000	43.7688	57.7725	1.7709	10.8622
0.7717	0.4735	0.0000	43.7347	57.7395	14.2982	10.8614
0.6916	0.7875	0.0000	43.7667	57.7725	8.0701	10.8704
0.6154	1.0737	0.0000	43.7760	57.7769	1.0937	10.8654
3.1408	0.3921	0.0000	14.4126	54.2684	14.9817	29.6905
1.3780	0.4234	0.0000	43.8312	57.8478	14.9899	22.4737
0.7510	0.5374	0.0000	43.6938	57.6969	12.7630	10.8832
0.7619	0.5011	0.0000	43.7273	57.7321	13.6115	10.8592
0.7885	0.4417	0.0000	42.4540	56.6538	14.9826	11.1616
2.5384	0.3997	0.0000	27.6294	54.2225	14.9860	29.6479
0.6476	0.9777	0.0000	43.7858	57.7862	4.3451	10.8405
0.6539	0.9605	0.0000	43.7268	57.7618	4.6874	10.8737
0.7302	0.6162	0.0000	43.7600	57.7742	11.1410	10.8701
1.4350	0.4230	0.0000	44.0176	58.0291	14.9530	23.5120
0.7456	0.5543	0.0000	43.7295	57.7353	12.3993	10.8613
2.4693	0.3997	0.0000	28.7994	54.2191	14.9860	29.6718
0.6829	0.8295	0.0000	43.7709	57.7744	7.3523	10.8684
2.8919	0.3930	0.0000	20.3865	54.0438	14.9753	29.6891
2.9550	0.3922	0.0000	19.9865	54.2225	14.9909	29.9571
1.2832	0.4297	0.0000	43.8136	57.8417	14.9383	20.6248
1.7245	0.4034	0.0000	43.9677	58.0046	14.9936	29.1031
0.6822	0.8405	0.0000	43.7701	57.8037	7.1727	10.8684
0.6619	0.9353	0.0000	43.7307	57.7625	5.4445	10.8690
2.8919	0.3930	0.0000	20.3865	54.0438	14.9753	29.6891

Table B.1. Continued

Mass Ratio	Pitch Frequency Ratio	Constraint Function	P1	P2	P3	P4
0.6634	0.9193	0.0000	43.7747	57.7781	5.7591	10.8444
0.6315	1.0416	0.0000	43.7588	57.7835	2.6211	10.8640
0.7757	0.4614	0.0000	43.7288	57.7321	14.6153	10.8566
1.5997	0.4120	0.0000	44.0176	58.0236	14.9505	26.7285
0.6358	1.0248	0.0000	43.7760	57.7769	3.1207	10.8654
0.6893	0.7984	0.0000	43.7712	57.7761	7.8859	10.8685
0.7691	0.4818	0.0000	43.7293	57.7423	14.0892	10.8614
2.7339	0.3965	0.0000	24.5597	54.2257	14.9887	29.9363
2.7866	0.3955	0.0000	22.7732	54.0840	14.9786	29.6886
1.7245	0.4034	0.0000	43.9677	58.0046	14.9936	29.1031
1.7698	0.4009	0.0000	43.9677	58.0237	14.9936	29.9379
0.7185	0.6601	0.0000	43.7380	57.7413	10.3011	10.8666
0.7217	0.6466	0.0000	43.7373	57.7420	10.5526	10.8656
0.7217	0.6466	0.0000	43.7373	57.7420	10.5526	10.8656
0.6269	1.0516	0.0000	43.7675	57.7725	2.2637	10.8622
2.7866	0.3955	0.0000	22.7732	54.0840	14.9786	29.6886
1.2832	0.4297	0.0000	43.8136	57.8417	14.9383	20.6248
0.7581	0.5131	0.0000	43.7306	57.7334	13.3249	10.8626
0.7017	0.7382	0.0000	43.7723	57.7744	8.9163	10.8696
0.7094	0.7052	0.0000	43.7805	57.7849	9.4940	10.8768
0.7361	0.5898	0.0000	43.7293	57.7413	11.6607	10.8613
0.7391	0.5788	0.0000	43.7356	57.7413	11.8829	10.8669
0.6087	1.0807	0.0000	43.7763	57.7769	0.4020	10.8653
0.6893	0.7984	0.0000	43.7712	57.7761	7.8859	10.8685
0.6822	0.8405	0.0000	43.7701	57.8037	7.1727	10.8684
0.6829	0.8295	0.0000	43.7709	57.7744	7.3523	10.8684
0.7666	0.4873	0.0000	43.7269	57.7321	13.9486	10.8592
0.7640	0.4944	0.0000	43.7310	57.7321	13.7726	10.8591
0.6321	1.0366	0.0000	43.7756	57.7764	2.7787	10.8633
0.6259	1.0542	0.0000	43.7688	57.7725	2.1627	10.8622

BIOGRAPHY OF THE AUTHOR

Hannah Allen was born in Farmington, Maine on April 15, 1993. She was raised in Farmington, Maine and graduated from Mount Blue High School in 2011. Following her high school graduation Hannah decided to pursue a Bachelor of Science degree in Mechanical Engineering at the University of New Haven. In May 2015, Hannah completed her Bachelor's degree in Mechanical Engineering with a minor in Sustainability Studies with cum laude honors. Upon completion of her Bachelor's degree, Hannah worked in military jet engine limits design until moving on to pursue her passion in sustainability. Hannah returned to Maine to study mechanical engineering at the University of Maine while researching floating offshore wind turbine hulls. Hannah is a candidate for the Master of Science degree in Mechanical Engineering from the University of Maine in May 2019.